Lens Based Kinetic Inductance Detectors With Distributed Dual Polarized Absorbers for Far Infrared Space-Based Astronomy

Shahab Oddin Dabironezare, *Member, IEEE*, Giulia Conenna, Daan Roos, Dimitry Lamers, Daniela Perez Capelo, Hendrik M. Veen, David J. Thoen, Vishal Anvekar, Stephen J. C. Yates, Willem Jellema, Robert Huiting, Lorenza Ferrari, Carole Tucker, Sven L. Van Berkel, *Member, IEEE*, Peter K. Day, Henry George Leduc, Charles M. Bradford, Nuria Llombart, *Fellow, IEEE*, and Jochem J. A. Baselmans

***Abstract*—Future space-based far infrared astronomical observations require background limited detector sensitivities and scalable focal plane array solutions to realize their vast potential in observation speed. In this work, a focal plane array of lens absorber coupled kinetic inductance detectors (KIDs) is proposed to fill this role. The figures of merit and design guidelines for the proposed detector concept are derived by employing a previously developed electromagnetic spectral modeling technique. Two designs operating at central frequencies of 6.98 and 12 THz are studied. A prototype array of the former is fabricated, and its performance is experimentally determined and validated. Specifically, the optical coupling of the detectors to incoherent distributed sources (i.e., normalized throughput) is quantified experimentally with good agreement with the estimations provided by the model. The coupling of the lens absorber prototypes to an incident plane wave, i.e., aperture efficiency, is also indirectly validated experimentally matching the expected value of 54% averaged over two linear polarizations. The noise equivalent power of the KIDs is also measured with limiting value of 8×10^{-20} W$/\sqrt{\text{Hz}}$ at the bath and radiator temperatures of 130 mK and 2.7 K, respectively, under negligible optical loading.**

Received 3 June 2025; revised 4 August 2025; accepted 29 August 2025. Date of publication 16 September 2025; date of current version 23 December 2025. *(Corresponding author: Shahab Oddin Dabironezare.)*

Shahab Oddin Dabironezare, Daan Roos, and Jochem J. A. Baselmans are with the Terahertz Sensing Group, Delft University of Technology, 2628CD Delft, The Netherlands, and also with Space Research Organisation Netherlands, 2333 CA Leiden, The Netherlands (e-mail: s.o.dabironezare-1@tudelft.nl; j.j.a.baselmans-1@tudelft.nl).

Nuria Llombart is with the Terahertz Sensing Group, Delft University of Technology, 2628CD Delft, The Netherlands (e-mail: n.llombartjuan@tudelft.nl).

Giulia Conenna, Dimitry Lamers, Daniela Perez Capelo, Hendrik M. Veen, David J. Thoen, Vishal Anvekar, and Robert Huiting are with Space Research Organisation Netherlands, 2333 CA Leiden, The Netherlands (e-mail: g.conenna@sron.nl; d.lamers@sron.nl; d.perez@sron.nl; m.veen@sron.nl; d.j.thoen@sron.nl; v.anvekar@sron.nl; r.huiting@sron.nl).

Stephen J. C. Yates, Willem Jellema, and Lorenza Ferrari are with Space Research Organisation Netherlands, 9747 AD Groningen, The Netherlands (e-mail: s.Yates@sron.nl; w.jellema@sron.nl; l.ferrari@sron.nl).

Carole Tucker is with the School of Physics and Astronomy, Cardiff University, CF24 3AA Cardiff, U.K. (e-mail: caroletucker@celtic-thz.co.uk).

Sven L. Van Berkel, Peter K. Day, Henry George Leduc, and Charles M. Bradford are with Jet Propulsion Laboratory, La Cañada Flintridge, CA 91011 USA (e-mail: sven.l.van.berkel@jpl.nasa.gov; peter.k.day@jpl.nasa.gov; henry.g.leduc@jpl.nasa.gov; charles.m.bradford@jpl.nasa.gov).

This article has supplementary material provided by the authors and color versions of one or more figures available at https://doi.org/10.1109/TTHZ.2025.3610552.

Digital Object Identifier 10.1109/TTHZ.2025.3610552

***Index Terms*—Distributed absorber, far infrared, kinetic inductance detector (KID), lens focal plane array, space-based astronomy.**

I. Introduction

THE far-infrared (FIR) part of the electromagnetic (EM) spectrum contains unique information on cosmological processes, which are mostly unavailable at other wavelengths, while containing a significant portion of the energy emitted within the universe [1]. At this moment, no astronomical instrument targets a critical portion of this spectrum, with a wavelength range of 25–300 μm (1 − 12 THz). Since Earth's atmosphere is mostly opaque for EM waves between 1 and 12 THz, a ground-based instrument is not a feasible solution. Passively cooled space-based telescopes will reach temperatures down to $\simeq$ 50 K, resulting in self-emission of thermal radiation far exceeding the universe background in the FIR. Only an actively cooled ($<$ 5 K) space-based telescope, in combination with extremely sensitive detectors with noise equivalent power (NEP) values below 10^{-19} W$/\sqrt{\text{Hz}}$, will be able to detect background limited radiations. Such an instrument would allow for a massive increase in spectral observing speed in the order of 10^5 with respect to existing instruments [2].

The probe far-infrared mission for astrophysics (PRIMA) [3], [4] is a NASA led FIR mission aiming to close the EM observation gap between ground-based instruments such as ALMA and the space-based mid-infrared instrument of the James Webb Space Telescope by providing background limited radiation detection using actively cooled optics. The PRIMA observatory would contain multitude of functionalities using an imager, PRIMAger [5], and a grating spectrometer, FIRESS [6], for spectroscopical measurements.

Only superconductor-based detectors such as transition-edge sensors [7], [8], quantum capacitor detectors [9], and kinetic inductance detectors (KID) [10] are possible solutions to the extreme sensitivity requirements for PRIMA and comparable missions with actively cooled optics. Between these three archetypes of superconductor detectors KIDs have the benefits of the following:

1) allowing for large, sensitive arrays with $\sim 10^3$ detectors read-out using a single back-end [11], [12];
2) reaching the required sensitivities, corresponding to limiting NEP values of $3 \cdot 10^{-20}$ W$/\sqrt{\text{Hz}}$ at 1.5 THz [13] and $4.6 \cdot 10^{-20}$ W$/\sqrt{\text{Hz}}$ at 12 THz [14];
3) fairly matured technology employed in stratospheric balloon instruments [15], [16];
4) resilience to fluctuations in the temperature of the background and focal plane array (FPA) due to lacking a limiting saturation threshold; and
5) indications for tolerance against cosmic ray interactions, with a low estimated loss in integration efficiency due to cosmic rays in an orbit at the second Lagrange point of the Earth–Sun system (L2) [17], as well as indications that a total ionising dose for a 5 year operation in L2 (estimated as 29Gy for a Silicon wafer of 20 mm $\times$ 20 mm$\times$350 μm) has no measurable effect on device performance [18].

KIDs are planar superconducting resonators, capable of absorbing THz radiation, operating at a temperature $\simeq T_c/10$, where T_c is the critical temperature of the superconductor. Under these conditions all charge carriers are condensed in a Bose–Einstein condensate of Cooper pairs, which transport charge without any resistance, but with a finite inductance due to Cooper pair inertia called "kinetic inductance." Radiation at a frequency exceeding the gap frequency [90 GHz for aluminium (Al)] will break Cooper pairs into quasiparticle excitations. This process increases both the losses and the kinetic inductance [10], which will change the resonant frequency and quality factor of the resonator. A KID is, therefore, a microwave resonator in which an EM radiation coupling structure is embedded that allows for efficient radiation absorption. This latter is typically an antenna or absorber, whereas the rest of the resonator can be a various combination of distributed or lumped elements, creating a resonator operating typically in a frequency band of 0.5–8 GHz.

In antenna-based KIDs EM radiation is captured, transformed into a guided wave, which propagates through a transmission line, and finally absorbed within the resonator part of the KID. In contrast, in an absorber-based KID, EM radiation is directly absorbed at the EM sensitive part of the detector, which is also part of the resonator. Antenna coupled KIDs, e.g., based on standard horns and leaky lenses, exhibit better coupling control to incoming EM radiation due to their spatial filtering capability [19]. However, these detectors require a coupling mechanism to transform the impinging wave, captured by the antenna, to a guided wave for absorption at the KID. This requirement adds to the complexity of antenna-based devices. On the other hand, specifically relevant at high THz (> 5 THz) frequencies, an absorber-based KID, entirely removes the complexities of coherent coupling to a THz transmission line. Moreover, the fabrication and assembly tolerances are significantly relaxed in such a detector with respect to the antenna case, since former is an incoherent detector and not sensitive to the phase of the incoming radiation.

Distributed bare absorbers have been employed as lumped element KIDs in instruments such as [16], [20] and [21] where the inductive part of the KID's resonator doubles as the radiation absorbing structure. By introducing a focusing dielectric lens component on top of the absorbers, as shown in Fig. 1(a), the size of the absorber can be reduced, limited to the focal spot of the lens, leaving room to freely design the resonator's capacitive section without reducing the array fill factor. Moreover, the presence of a dielectric lens on top of the absorber acts as an additional spatial filter, which reduces the sensitivity of the detector to stray light absorption with respect to a bare absorber design.

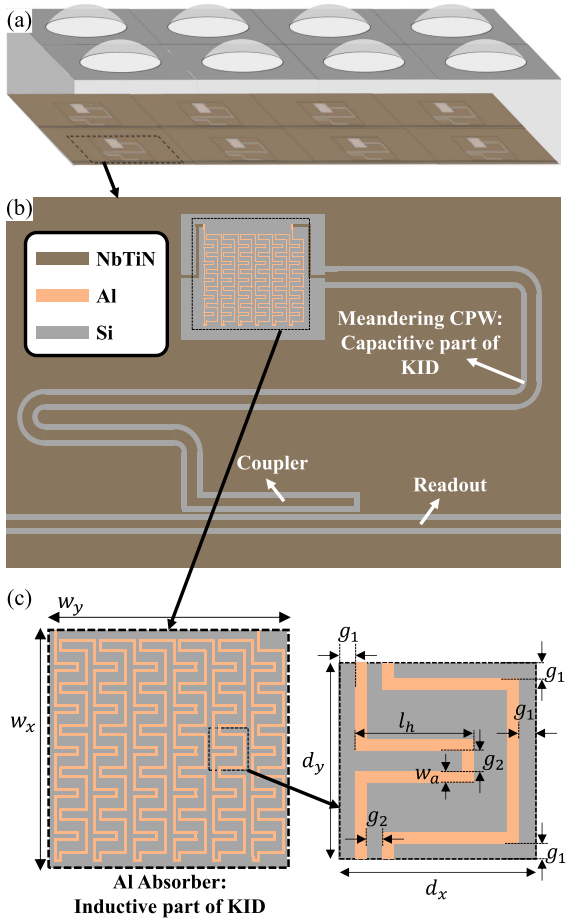

Fig. 1. Schematic representation of the geometry under investigation. (a) Integrated elliptical lens array with absorber coupled KIDs placed over its focal plane. (b) Zoomed in view of a detector geometry consisting of a distributed absorber connected to a quarter wavelength CPW resonator. The inductive (absorber) part of the KID is short circuited while the capacitive part (CPW) is terminated with an open-circuit coupler. (c) Tightly packed periodic absorber array, its unit cell and design parameters.

In this work, we present the design and experimental validation of lens-absorbers-based KIDs. We employ a spectral model to codesign the absorbers and lenses, resulting in a very efficient and fast design process. Such a design is simply not achievable resorting only to full wave simulators. This method is built upon the work in [22]; derived in [19] for bare absorbers below a parabolic reflector, in which we drew comparisons to antenna-based systems and showed detailed validations against full wave simulations; and experimentally validated for an bolometer in [23]. The technique can be readily extended to entirety of an imaging system via [24] to optimize the observation speed of an

instrument as investigated in [25]. Our design employs a unit cell with two parallel meandering narrow Al lines, which provides a wide operational bandwidth, high coupling efficiency, and dual polarized response. We focus on designs at two frequency bands, relevant to the PRIMAger instrument, centred at 6.98 and 12 THz. Furthermore, the end-to-end performance of the 6.98 THz design is evaluated by fabricating a 25-KID array and measuring their NEPs and optical couplings to an incoherent distributed source (also referred to as the normalized throughput in the literature [26], [19]).

The rest of this article is organized as follows. Section II contains guidelines to codesign distributed absorber structures below integrated lens components with a detailed performance study over the relevant design parameters. In Section III, the designed lens absorber coupled KID geometries are presented. Section IV is focused on the experimental characterization of the fabricated devices and comparison to the ones estimated by the model. Finally, Section V concludes this article. The EM figures of merit of a lens absorber are reviewed in Appendix A. The additional data regarding the EM performance of the designed lens absorbers are provided in Appendix B. The analytical expressions for designing the coplanar waveguide (CPW) section of the KIDs are provided in Appendix C. The experimental setup is provided in Appendix D. In Appendix E, the steps taken to model and experimentally quantify the optical coupling for a multimode detector is formulated. The additional experimentally obtained data are given in Appendix F. In the accompanying Supplementary Material, a tolerance study, relevant for development of detectors at FIR wavelengths, is provided on lens absorber geometries.

II. Lens Absorber Design Guidelines

Based on a previously developed spectral modeling technique, [22] and [19], this section is focused on the codesign guidelines for lenses and distributed absorbers. In this article for brevity, the latter is referred to as absorber. The guidelines provided in this section are employed to design and evaluate the performance of the lens absorber prototype in Section III.

Detector arrays for an FIR space observatory will have multiple possible functionalities such as spectroscopy, polarimetry, and imaging [4]. The lens FPAs will be typically placed below reflector chains with a large (> 10) equivalent focal to diameter (f-number) ratio. Large f-number requirements and tight sampling for the lens FPA permits us to consider a study in which an incident plane wave directly illuminates the lens FPA (see Fig. 2), and to focus on demonstrating the performance of lens absorber components in isolation. As a result, the considered design parameters here are not the lens diameter (sampling rate below the reflector system), nor the design of the reflector chain and its equivalent f-number. Such parameters can be designed for specific observation scenarios based on guidelines in [25]. Instead, here we focused on the lens f-number, absorber size, absorber unit cell design, and KID design.

A. EM Response of a Lens Absorber to Incident Plane Waves

Our absorber design consist of a finite array of lossy unit cells. The absorption response of a tightly periodic array of unit cells

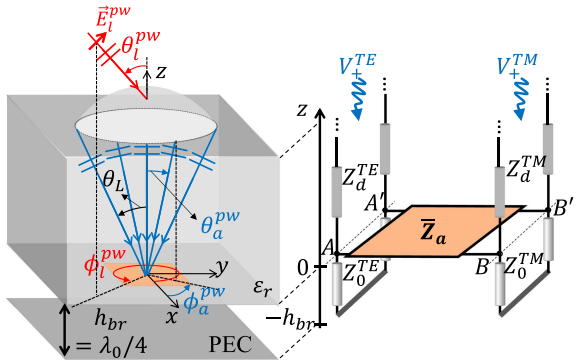

Fig. 2. Example lens absorber geometry with quarter wavelength backing reflector (left-hand side) and its equivalent Floquet wave model (right-hand side). The lens is illuminated by an incident plane wave from θ_l^{pw}, ϕ_l^{pw} direction, its subtended angle is limited to θ_L, and its focal field is model as a PWS. The absorber is modeled as a two-port impedance network containing its spectral response to plane waves arriving from each θ_a^{pw}, ϕ_a^{pw} combination of angles.

to an incident plane wave can be estimated via the fundamental Floquet wave modes while neglecting finiteness effects. In this work, this response is referred to as the *spectral response* of an absorber. This response can be derived analytically for simple geometries such as resistive sheets and strip absorber arrays, as in [19] and [27], respectively. For arrays with a complex unit cell geometry, one can obtain this response numerically using the periodic boundary conditions in a full wave simulator, e.g., CST MS [28], as in [23]. The Floquet wave model is shown in Fig. 2 for an incident plane wave illuminating the absorber from colatitude and azimuth angles, θ_a^{pw} and ϕ_a^{pw}, respectively. The model contains an equivalent transmission line with two ports and generators, transverse electric (TE) and transverse magnetic (TM) fundamental Floquet modes, representing the stratification and incident plane waves. The absorber's response is included as a two-port impedance network, $\bar{Z}_a$.

The response of a focusing quasi-optical (QO) component to an incident plane wave, i.e., the focal field generated from this plane wave, can be represented as a summation of plane waves, referred to as direct plane wave spectrum (PWS) [22]. The term *direct* indicates that the field distribution is obtained without the presence of the absorber. This PWS is limited to the focusing component's maximum subtended angle, θ_L (see Fig. 2). The field distribution with inclusion of the absorber's spectral response is referred to as the *total* PWS. This PWS is constructed by solving the described Floquet wave circuit per spectral direction. By coherently summing the total PWS, the total spatial fields at the area containing the absorber are obtained. The Poynting vector associated to these fields is then integrated over the absorber's physical domain to calculate the power absorbed [19]

$$P_{\text{abs}}\left(f, \theta_l^{\text{pw}}, \phi_l^{\text{pw}}\right) = \frac{1}{2}\Re\left\{\iint_{-w/2}^{w/2} [\vec{e}_t(\vec{\rho}, \theta_l^{\text{pw}}, \phi_l^{\text{pw}}) \times \vec{h}_t^*(\vec{\rho}, \theta_l^{\text{pw}}, \phi_l^{\text{pw}})] \cdot \hat{z}\, \mathrm{d}\vec{\rho}\right\} \tag{1}$$

where f is the photon frequency, θ_l^{pw} and ϕ_l^{pw} are the colatitude and azimuth angles, respectively, of the incident plane wave

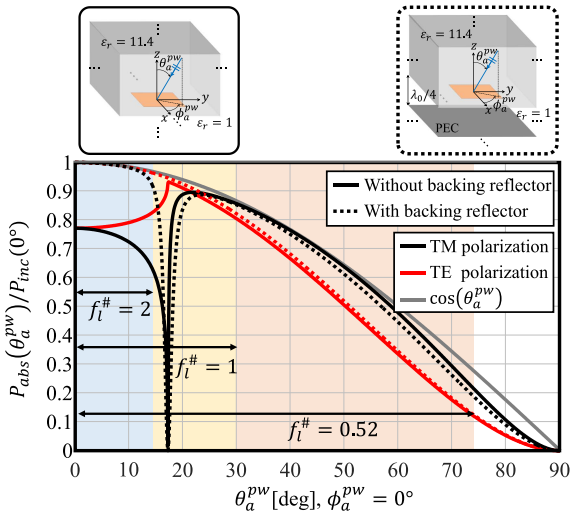

Fig. 3. Spectral response (absorption rate) of ideal absorbers with or without quarter wavelength backing reflector are shown as a function incident plane wave angles. These plane waves are propagating within a semi-infinite silicon slab and the absorber is located at air-silicon interface. The angular regions corresponding to the three considered lens f-number cases are also marked.

illuminating the lens, w is the side length of an square domain absorber, $\vec{e}_t$ and $\vec{h}_t$ are the total electric and magnetic spatial fields, respectively, evaluated over the focal plane of the lens at $\vec{\rho} = x\hat{x} + y\hat{y}$ locations. Equation (1) quantifies the amount of power the absorber receives from point sources located at θ_l^{pw} and ϕ_l^{pw} angular location outside the lens. Relevant figures of merits, derived in [19] for a bare absorber below an equivalent parabolic reflector, are briefly reviewed in Appendix A for lens absorbers.

B. Codesign of the Lens-Absorber

Let us consider two idealized absorber geometries coupled to silicon integrated lenses to investigate the tradeoffs present in such geometries. i) An absorber with equivalent sheet resistance of $R_s = \zeta_d||\zeta_0\ \Omega/\square$ placed at the air-silicon interface, where ζ_d is the characteristic impedance of the high-resistivity silicon at cryogenic temperatures (with permittivity of $\varepsilon_r = 11.44$) and ζ_0 is the impedance of free space; ii) an absorbing structure with $R_s = \zeta_d\ \Omega/\square$ placed at the air-silicon interface above a quarter wavelength backing reflector. The spectral response of these two ideal absorbers is shown in Fig. 3, similar to the one in [22], with the insets indicating their stratification. The response of both is limited to the cosine law of Lambert, while the cases without or with the backing reflector have maximum broadside absorption rates of 77% and 100%, respectively. In both stratification cases, a null exists in the TM polarized response at the critical angle value corresponding to the air-silicon interface.

In Fig. 3, the angular regions subtended by three example lens elements are also marked. Here, silicon lenses with three f-numbers are considered:

1) shallow truncated elliptical lens with $f_l^{\#} = 2$ and $\theta_L = 14.5°$;
2) a moderately truncated lens with $f_l^{\#} = 1$ and $\theta_L = 30°$; and
3) an untruncated ellipsoid with $f_l^{\#} = 0.52$ and $\theta_L = 74°$.

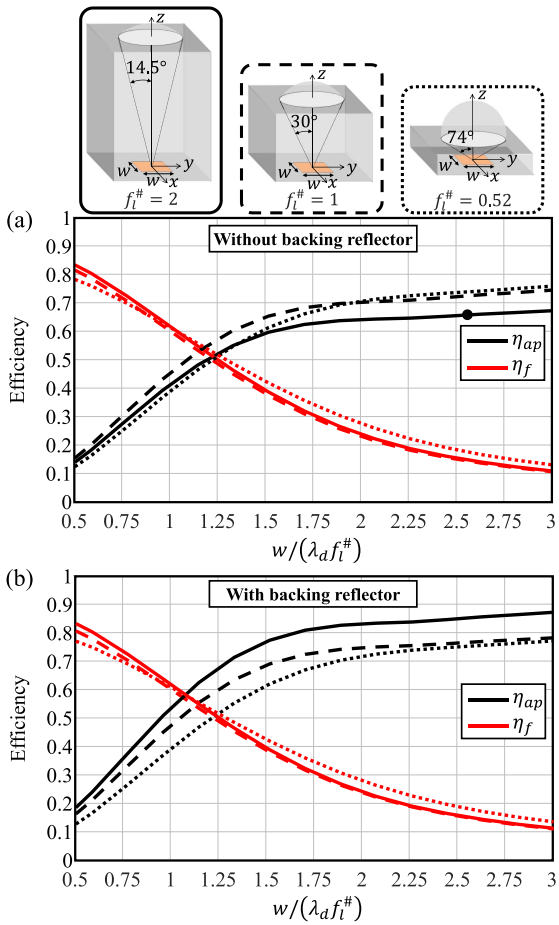

Fig. 4. Aperture and focusing efficiencies as a function of absorber sampling rate for three lens f-number cases: ideal absorber (a) without, and (b) with quarter wavelength backing reflector. The example incident plane wave illuminating the lenses is y-polarized. Solid, dashed, and dotted lines correspond to lens f-numbers of 2, 1, and 0.52, respectively. The top insets indicate these lens geometries. The black colored circle in (a) theoretical limit of the aperture efficiency for the fabricated prototype.

The lens absorber's performance in terms of aperture and focusing efficiencies are plotted in Fig. 4 by varying the absorber side length for the three considered elliptical silicon lenses. Standard quarter wavelength antireflection coatings are considered on the lenses.

A constant and equal to one spectral response, instead of the ones shown in Fig. 3, for an absorber within its lens subtended angle leads to a total PWS equal to the direct PWS. A focal field constructed from coherently summing the direct PWS have the narrowest possible main beam, which approaches the one of the Airy pattern for lenses with large f-numbers. Such a narrow focal field in turn is equivalent to absorbing more power from the intended source direction with a fixed absorber size. However, a unitary spectral response is not feasible due to the cosine law but approaching it is the design goal of absorber unit cells. The enhancement of the aperture efficiency for an ideal absorber with backing reflector below a lens with $f_l^{\#} = 2$, solid black colored

curve in Fig. 4(b), showcases this goal since the spectral response of this absorber is relatively unitary within the angular region of its lens (see Fig. 3). In contrast, for cases without backing reflector, lenses with larger subtended angular regions achieve higher aperture efficiencies due to the presence of a maximum in the absorber's spectral response outside the angular domain of the $f_l^{\#} = 2$ lens.

In terms of the angular selectivity of the lens absorber, modifying the lens f-number and absorber's spectral response leads to minute variations while the absorber's size dominates the behavior. This is shown in Fig. 4 by comparing the focusing efficiencies for ideal absorbers below lenses with different f-numbers and spectral responses. In Fig. 14 in Appendix A, the same behavior is shown in terms of widening of the normalized reception power pattern when larger (in terms of $\lambda_d f_l^{\#}$, where λ_d is the wavelength in silicon) absorbers are placed below a lens.

To summarize, the tradeoffs between focusing and aperture efficiencies dictates a specific design guideline: the absorber's spectral response and the lens angular domain should be codesigned to achieve the highest aperture efficiency using the smallest possible absorber normalized (in terms of $\lambda_d f_l^{\#}$) size. Such an approach leads to maximizing the power received from the intended source direction (high η_{ap}), and reducing the detector's sensitivity to stray light and sky background radiations (high η_f), i.e., increasing the signal power while receiving the smallest amount of background noise.

It is worth emphasizing that an approach similar to the one discussed in this section is feasible for analyzing and codesigning a complete lens absorber FPA coupled to a reflector QO system. This can be achieved by obtaining the direct PWS of the cascaded focusing system using the formulations derived in [24] by combining a numerical Geometrical Optics technique with the Coherent Fourier Optics approach.

III. Detector Design

In this section, we present the design of two lens-absorber geometries operating at central frequencies of 6.98 and 12 THz. We provide their design parameters and estimate their performance in terms of aperture efficiency and reception power pattern. In Section III-A, we present the absorber's unit cell design and spectral response, and in Section III-B, the lens-absorber design. In Section III-C, we discuss the integration of the absorber into a microwave resonator to complete the KID design.

A. Absorber Unit Cell Design

We first study the properties of Al films. In Fig. 5, we show the complex surface impedance of three Al films with thickness of τ and resistivity of ρ_{res}, using expressions given in [29] and the measured dc resistance at 1.5 K given in the legend. As can be seen, the sheet reactance of Al cannot be neglected with respect to its resistance at FIR wavelengths. As a result, a standard strip absorber design, as shown in [27], will have a significant reactance and will be practically impossible to match to the (real) impedance of the FIR radiation on the Si-air interface. Even matching the real part of the impedance of such an absorber

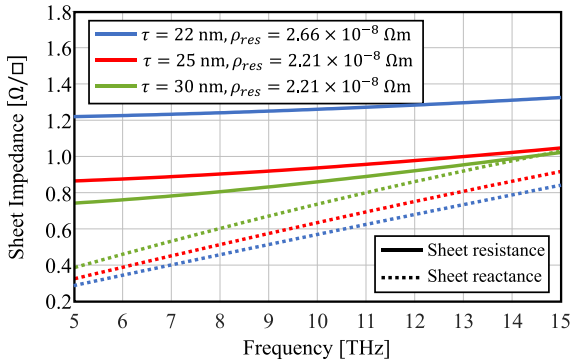

Fig. 5. Sheet impedance of example Al films deposited on silicon substrate with τ thickness and dc resistivity of ρ_{res}. These resistivity values are calculated from the measured dc resistance of Al test strips at 1.5 K, and sheet impedances are calculated based on the model in [29].

TABLE I
Design Parameters of the Two Absorber Geometries [See Fig. 1(c)] Given in μm

Absorber type	Hor. side length w_x	Ver. side length w_y	Hor. period d_x	Ver. period d_y	Strip width w_a	Hor. meander length l_h	Gap width g_1	Gap width g_2
6.98 THz	64	61.6	6.4	7.7	0.3	3.8	0.3	0.5
12 THz	38.7	38.4	4.3	4.8	0.25	2.3	0.25	0.5

is not feasible in practice: it would require extremely narrow (< 100 nm) and thin (< 10 nm) strips, which are unattainable in fabrication and would significantly reduce the maximum microwave readout power handling of the KIDs. In this work, we propose a unit cell consisting of two meandering Al strips, explored in [30] to develop dual polarized absorbers, which is employed here to achieve relatively wide band impedance matching at THz frequencies using Al. The proposed design is shown in Fig. 1(c). The advantage of this design with two meandering strips over a single one [14] is a wider bandwidth, which additionally results in an increased tolerance to variations in the width of fabricated lines as well as variations in the resistivity of Al films.

By optimizing the geometrical parameters of the proposed unit cells, one can quasi-independently tune the impedance of the structure seen by TE and TM polarized plane waves. Such a structure has a resonant behavior due to the combination of the capacitive and inductive responses of a dual meandering strip [30] with the Al sheet impedance. As a result, it provides a large degree of freedom to tune the frequency response of the absorber. We have concluded from the optimization process that narrower and thinner Al strips lead to wider operation bandwidths. However, both of these requirements lead to a more challenging fabrication process. As a result, the Al thicknesses chosen for 6.98 and 12 THz absorber designs are 22 nm with a dc resistivity of about 2.66×10^{-8} Ωm.

The geometrical parameters of the unit cells operating at the two frequency bands are reported in Table I. The absorbers discussed here are designed without the inclusion of a quarter wavelength backing reflector to reduce the fabrication complexity of the initial prototypes. The spectral response of these

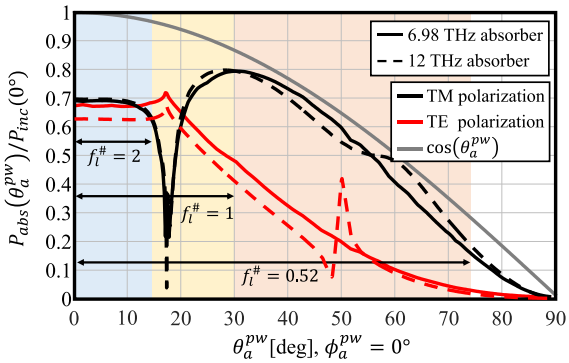

Fig. 6. Spectral response of the proposed absorber unit cells to incident plane waves at $\phi_a^{\mathrm{pw}}=0°$ cut. The indicated angular regions correspond to the three considered lens f-number cases.

absorbers at the centre of their operation band is shown in Fig. 6. A tight periodicity was enforced in the designs to limit the absorber's spectral response to only fundamental TE and TM Floquet waves. As a result, scan blindness does not occur over the operation bands and within the angular domain subtended by the truncated elliptical lenses. By employing lens elements with limited angular domains, extreme tight periodicity requirements on the absorber unit cell could be relaxed. For the described designs, the presence of a higher order TE Floquet mode is noticeable in Fig. 6 for the 12 THz absorber at angles above $50°$. However, the influence of this mode on the performance of the absorber below an untruncated lens is negligible due to the damping of the response by the cosine law at large skewed angles.

B. Lens Absorber Design

The lens f-number and absorber array's side length were codesigned to satisfy the following criteria: experimentally demonstrating the aperture efficiency estimated by the model while reducing the risks associated with realization inaccuracies for the initial prototype. Consequently, a tolerance study was performed to estimate how sensitive is the aperture efficiency to the following four relevant issues at FIR wavelengths:

1) curvature inaccuracies in fabrication of the elliptical lens surface;
2) surface roughness of the lens;
3) lateral and vertical misalignments between the centre of the absorber array and the lens lower focus; and
4) the presence of air gaps in the silicon wafer stacks.

This study is provided in the Supplementary Material accompanying this article.

Based on the conclusions of the tolerance study and the estimated performance of lens absorber designs, together with the requirements for PRIMAger, lens elements with f-number $\simeq 2$ and a diameter of $D_l = 700$ μm were chosen. Moreover, absorbers with side lengths of $w \simeq 2.55\lambda_d f_l^{\#}$ are fabricated due to their tolerance to alignment errors. The absorber side lengths, in μm, are also provided in Table I.

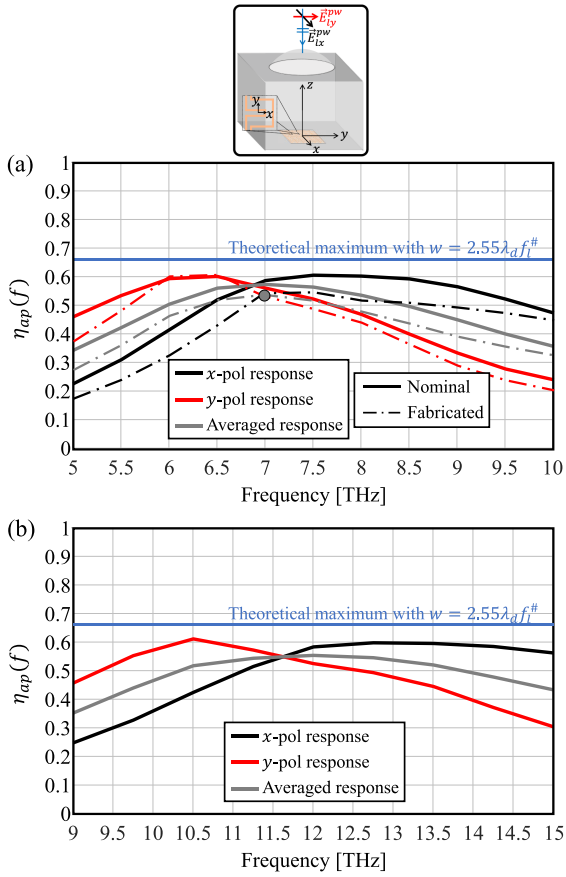

Fig. 7. Aperture efficiency of the designed (a) 6.98 and (b) 12 THz lens absorbers against their frequency of operation when the lens is illuminated by a x- or y-polarized plane wave from broadside direction. The averaged response to a combination of the two linear polarizations is also provided. The solid and dotted lines correspond to the designed and fabricated devices, respectively. The blue solid lines indicate the theoretical maximum value based on Fig. 4(a).

Lens absorber performance in terms of aperture efficiency over their operation frequency bands is reported in Fig. 7. The aperture efficiency of the two designs averaged over the two linear polarizations exhibits a maximum aperture efficiency about 15% below the theoretical maximum, and a 1 dB bandwidth of 3.2 and 5.1 THz (45.8% and 42.5% relative bandwidth) for 6.98 and 12 THz designs, respectively.

C. KID Design

The KIDs consist of the distributed absorbers, which act as both the THz sensitive section and a microwave inductor. The absorber is shorted to the chip ground on one side and connected to the central line of an open ended NbTiN CPW. With respect to Al, NbTiN is a superconductor with a larger energy gap, a lower quasiparticle generation efficiency, and lower quasiparticle lifetime. As a result, NbTiN is not a suitable choice for the THz sensitive section of the KID due to its low response. However, by employing an Al-NbTiN hybrid KID, one can trap the generated quasiparticles in a smaller Al volume which enhances the responsivity of the KID [31].

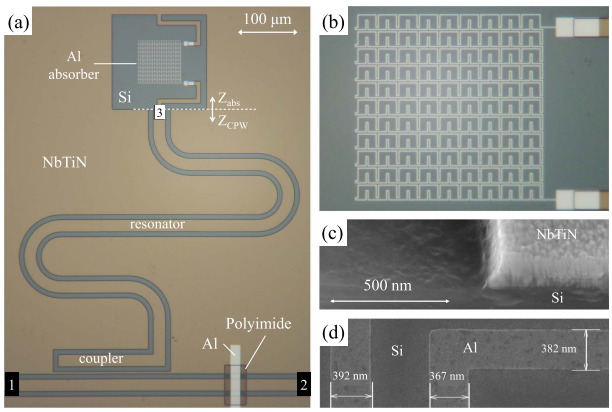

Fig. 8. (a) Optical micrograph of a single detector, indicating the CPW resonator, coupler, the bridge over the readout line and readout ports 1 and 2. The dash line and arrows indicate the port and de-embedding of the SONNET simulation for the absorber's input impedance. (b) Zoomed in on the absorber structure. (c) SEM image of the cross section of the NbTiN, showing the slope obtained during the etching step. This slope guarantees a good step coverage of the Al layer. (d) SEM image of a few lines of the absorber structure indicating the measured line widths.

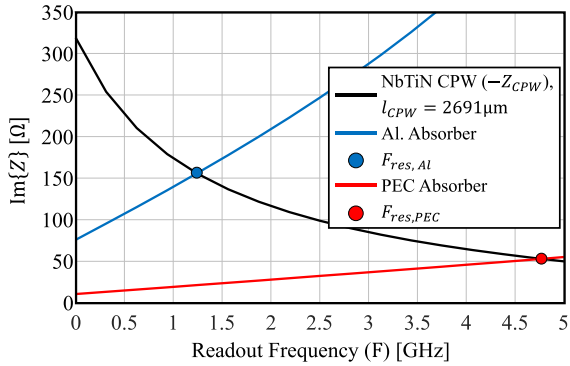

Fig. 9. Imaginary part of the input impedances of the 2 resonator sections, obtained at port "3" as shown in Fig. 8(a). The blue line shows Z_{abs} obtained using SONNET simulations using the measured parameters of the Al film, the red line is obtained by replacing Al with PEC. The black line gives the analytically calculated Z_{CPW} of the CPW line. The intersects give the resonant frequencies, we find $F_{\text{res}} = 1.94$ GHz for the Al absorber, and 4.80 GHz for the PEC case.

The device is read-out from port 1 to port 2 as indicated in Fig. 8(a). The NbTiN CPW has a (large) line width $S = 20\ \mu$m and (large) gap width $W = 8\ \mu$m to reduce the two level system noise of the KIDs [32]. The CPW length, l_{CPW}, is designed to tune the resonant frequency of the KID to the desired values between 2 and 4 GHz. Specifically, we simulated the input impedance of the absorber structure at microwave frequencies, (Z_{abs}), using a de-embedded port 3 as indicated in Fig. 8(a) in SONNET [33] and the dc resistivity and thickness of the Al. The reactive part of the Al's sheet impedance is negligible at the readout frequency range following its frequency dependency in the model, [29], and as can be inferred from Fig. 5. Subsequently, we analytically calculated the input impedance of the open ended NbTiN CPW line, Z_{CPW} from the same port, which is given by the standard expression

$$Z_{\text{CPW}} = Z_{\text{eff, NbTiN}} \cdot \cot\left(\frac{2\pi F}{v_{\text{ph}}} l_{\text{CPW}}\right) \tag{2}$$

where F is the readout frequency, $Z_{\text{eff, NbTiN}}$ is the effective NbTiN line impedance, and v_{ph} is the phase velocity of the line. The calculation of these parameters is detailed in Appendix C.

The resonant frequency, F_{res}, is given for the condition that the total imaginary impedance of the structure is 0, i.e., $\text{Im}\{Z_{\text{CPW}}\} + \text{Im}\{Z_{\text{abs}}\} = 0$. As an example, we give in Fig. 9, the result of this calculation for the lowest frequency KID in our test array, with the longest NbTiN CPW length (see Section IV). We repeat the calculation for the case where we replaced the Al with a perfect electric conductor (PEC) to obtain $F_{\text{res, PEC}}$. From these results, we can obtain the kinetic inductance fraction $\alpha_k = 1 - (F_{\text{res, Al}}/F_{\text{res, PEC}})^2 = 0.84$, which is defined as the fraction of the resonator's inductance due to the kinetic inductance of the Al. As mentioned, NbTiN section of the KID is not participating in the absorption of THz radiation by design; as a result, α_k term only includes the kinetic inductance of the Al section. Note that these calculations are based on the measured film parameters and geometries, which will be discussed together with the results presented in Section IV-B. Using this method, we designed a KID array with 25 KIDs in a hexagonal packing, with a spacing of 0.75 mm, with resonance frequencies within a 2.2–3.8 GHz readout frequency range, maintaining a constant fractional frequency difference $\text{d}F_{\text{res}}/F_{\text{res}} = 2.3 \cdot 10^{-2}$ between the resonators. Note that the design was done using estimated values of the dc resistance of the Al: a sheet resistance of $R_{s,\text{est}} \simeq 0.7\ \Omega/\square$ and $T_c = 1.4$ K.

IV. Experimental Verification

In this section, the fabrication, assembly, and experimental results corresponding to the lens absorber coupled KID design in Section III operating at the central frequency of 6.98 THz are discussed.

A. Fabrication and Assembly

We fabricate the devices on a 4 inch Float-Zone 350 μm $R_s \gg$ 10k Ω cm $<100>$ Si wafer. After standard wafer cleaning and a 10 s soak in 10% hydrogen fluoride, we deposit on the wafer backside a 35 nm thick β-Ta layer with $R_s \simeq 60\ \Omega/\square$, which is patterned using contact lithography and dry etching into a capacitive mesh as shown in Fig. 10(c). This layer will reduce the impact of cosmic rays [17] as well as the impact of stray radiation propagating through the chip [34]. Below each absorber location we leave a 300 μm diameter aperture to pass the beam from the lens array to the absorbers as sketched in Fig. 10(b). We subsequently deposit a 200 nm SiO2 sacrificial layer to keep the wafer backside pristine during subsequent processing steps. We then deposit a 150 nm thick NbTiN layer using reactive magnetron sputtering [35], which is patterned using contact lithography and dry etching in a $SF_6 - O_2$ plasma to create a $\simeq 60^\circ$ sloped edge, shown in Fig. 8(c). We measured the sheet resistance of the NbTiN $R_s = 17.9\ \Omega/\square$ and its critical temperature $T_c = 15.0$ K using a dc test chip from the same fabrication run and find that both values are identical to the expected ones. Afterwards,

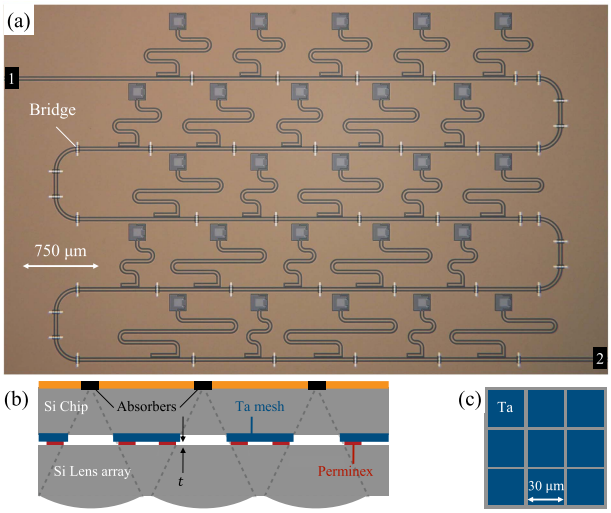

Fig. 10. (a) Micrograph of the entire KID array, showing 25 KIDs on a 0.75 mm pitch in a hexagonal packing. (b) Cross section of the assembled KID-lens array. The dashed lines indicated the radiation between the lenses and the absorbers, where no Ta mesh nor Perminex pillars are placed. (c) Pattern of the Ta mesh, creating a low-pass transmission making it invisible for signals at the KID readout frequency.

we create the support of the bridges over the CPW readout line to balance the ground planes. These bridges are needed to prevent crosstalk between KIDs due to mode conversion on the readout line [36]. This is done by spin, expose and cure of the photo-negative Fuji-film LTC9305 Polyimide. The last step is the fabrication of the Al absorber, including the contact pads to the NbTiN and the bridges [see Fig. 8(a) and (b)]. We use electron-beam evaporation through an methyl methacrylate—polymethyl methacrylate (MMA-PMMA) bilayer resist mask patterned using a Raith EBPG5200 electron beam pattern generator (EBPG) using a dose of 1050 μA/cm ^{2}. The exposed resist is developed using Methyl Isobutyl Ketone—Propanol 1:3 and etched for 30 s in an oxygen plasma to remove residual resist in the opened trenches. We then perform a 30 s buffered oxide etch (BOE): water 1:7 for 20 s to remove the oxide on the Si and NbTiN and deposit, using e-beam evaporation, a 22 nm thick Al layer. We measured on a 4-point dc chip from the same wafer $R_{s,\text{alu}} = 1.21\ \Omega/\square$, higher than the expected value, and a critical temperature $T_c = 1.4$ K, identical to the expected value. The sheet kinetic inductance of the Al is given by $L_s = 1.2$ pH calculated using $L_s = hR_s/(\pi\Delta)$, with $\Delta = 1.76k_BT_c$ [37] where k_B and h are the Boltzmann's and Planck's constants, respectively. The resist with obsolete Al is removed using a lift-off process in Dimethylformamide at 56° C for 1 h. This creates, in a single step, the Al absorber, with volume and area of 22.9 μm^3 and 1041 μm^2, respectively, as well as the contact to the NbTiN resonator. After this step, we remove the sacrificial SiO2 layer on the wafer backside using BOE while protecting the wafer front side with photoresist. This lifts-off any particles or contaminants created during the fabrication.

To prepare for mounting, we apply 500 nm thick layer of lithographically defined pillars made from Perminex 1001 on the chip backside, located only where they will not interfere with the radiation propagating from the lens array to the detector, schematically, as shown in Fig. 10(b). This creates a 500 nm vacuum gap between the lens array and chip, which is thin enough to maintain a good lens-absorber coupling, as shown in the Supplementary Material.

In Fig. 8, we show an optical micrograph of a single detector, and in its panel (d) a Scanning electron microscope (SEM) image of the absorber lines, which gives an average width of $w_a \simeq 380$ nm, 80 nm wider than designed values given in Table I. These wider lines also reduce the gap widths (g_1 and g_2) by 80 nm. The aperture efficiency due to this modified unit cell is shown in Fig. 7(a) by dash-dotted lines. In Fig. 10(a), we show the centre part of the detector chip under consideration, with 25 KIDs.

After fabrication, the wafer is diced in 20 mm $\times$20 mm chips, with standard optical AZ resist used as protection on the chip backside and PMMA resist on the chip metallization side. After dicing, we remove the backside protection using PN1000 developer, exposing the Perminex glue pillars. We mount the chip metal side down in an alignment tool, and align the chip to the lens array top, which is fabricated using laser ablation by Veldlaser [38] and antireflective coated with a 6.9 μm thick layer of Parylene-C [39], as a quarter wavelength matching layer. Note that we align on a marker on the lens array surface, which is displaced in z by 1.07 mm, from the chip markers, due to the thickness of the lens array.

After alignment, the chip and lens array are pressed together to create the required pressure of 0.58 MPa on the Perminex. We then bake the assembly in a preheated oven at 180 °C for 15 min. In this step, the chip and lens array reach a temperature exceeding 150°C for 5 min, which was evaluated in a test using thermal stickers. This creates a permanent bond between the chip and lens array. We remove the remaining front side PMMA using acetone.

B. Measured Performance

We mount the chip-lens array in a suitable holder, which is light tight, inside a completely light-tight box thermally anchored to the cold finger of an adiabatic demagnetization cooler [40] at 130 mK. To illuminate the detector array we use a thermal black body radiation source coupled to the 3 K stage of the cryogenic system, which can be heated up to 40 K. The black body, sample holder, and light tight box are equipped with a set of commercial metal mesh filters, consisting of two bandpass filters (BPF) and two high-pass filters (HPF) from Celtic Terahertz Ltd. defining a passband around 6.98 THz with extreme rejection at longer wavelengths. The total throughput from the radiator to the detector chip is defined by a 15 mm diameter aperture at 55 mm from the chip metallization side at the exit of the light tight box, which defines a full width opening angle of 15.95°. For a detailed description of this setup and its cross section, we refer to Appendix D and Fig. 18(a), respectively.

A key issue with the filter stack is that its in-band transmission is low, 25%, using the data provided by Celtic THz Ltd., which is obtained at 300 K. In our experiments, we use the filters at 4 K or 130 mK, where the dielectric and metallic losses will be lower than at 300 K. Hence, the in-band transmission will be higher

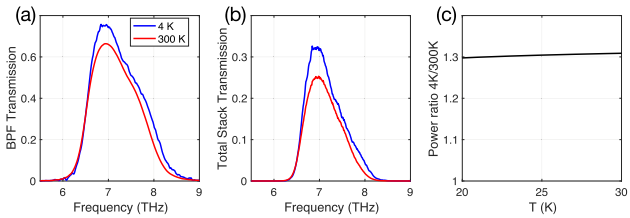

Fig. 11. (a) Room temperature and 4 K transmission for one BPF of our setup. (b) Room temperature and 4 K transmission for the entire filter stack of 2 BPF's and 2 HPF's. (c) Ratio of the power coupled to the detector for the 4 K data divided by the 300 K data as function of black body temperature within the T_{bb} temperature range of 20–30 K where we measure the optical efficiency.

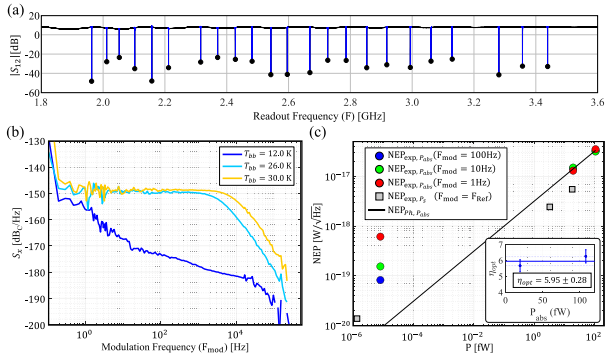

Fig. 12. (a) Frequency sweep at 130 mK and negligible radiator power showing 23 out of 25 KIDs. (b) Noise spectra for KID 10 $F_{\mathrm{res}} = 2.48$ GHz for the three radiator temperatures used in this experiment. (c) NEP as a function of absorbed power for KID 10, with in the inset the measured optical efficiency for the two higher radiator temperatures.

than based upon the 300 K data, which can lead to an overestimation of the coupling efficiency, as found in [13]. To eliminate as much as possible such a systematic error we measured a single BPF of our filter stack in a commercial Fourier-transform spectrometer at 4 K, the result is shown in Fig. 11(a). We observe a clear increase in transmission for the 4 K data, as well as a significant broadening of the filter bandwidth, coming from an upshift of the high-frequency edge. For the two HPF's in our setup we relied upon data from Celtic THz for a similar filter as the one we used. These measurements show only a 2.5% increase in transmission when going from 300 to 4 K. In Fig. 11(b), we show the resulting frequency dependent transmission of the *entire* filter stack (2 BPF's and 2 HPF's) at 4 K, together with the 300 K data as reference. In panel (c), we show the relative increase of the total transmission in the setup integrated over frequency for the black body temperature range where we will obtain the detector coupling efficiency. We observe an increase in power of 30% for the 4 K data with respect to the original 300 K filter data. It is noteworthy that this is only caused by the peak transmission increase, the upshift of the high-frequency edge has minimal effect as the Planck brightness of the radiator decreases exponentially for all black body temperatures plotted and the power transmitted is dominated by the low-frequency edge and the peak filter stack transmission.

In the first experiment, we measured the resonant frequency of all the KIDs at the bath temperature of $T_{\mathrm{Bath}} = 130$ mK and a radiator temperature of $T_{\mathrm{BB}} = 2.7$ K. At this temperature, the power radiated in-band is negligible [$\leq 10^{-23}$ W, as shown in Fig. 18(c) in Appendix D]. As can be seen from Fig. 12(a), we find 23 out of the 25 KIDs, which represent a yield of 92%, with a coupling quality factor $Q_c = 2.1 \pm 0.6 \cdot 10^4$ and internal quality factor $Q_i = 8.2 \pm 0.5 \cdot 10^6$. We also find that the fractional frequency spacing of the KIDs $\mathrm{d}F_{\mathrm{res}}/F_{\mathrm{res}} = 0.023 \pm 0.0019$ as designed. The standard deviation of the fractional frequency scatter, $\sigma_{\mathrm{d}F_{\mathrm{res}}/F_{\mathrm{res}}} = 1.9 \cdot 10^{-3}$ is an order of magnitude worse than the value reported by [41] of $\sigma_{\mathrm{d}F_{\mathrm{res}}/F_{\mathrm{res}}} = 1.8 \cdot 10^{-4}$, but obtained without post fabrication corrections. The lowest frequency resonator has $F_{\mathrm{res}} = 1.96$ GHz, very close to the calculated value based upon the measured film parameters and device geometry of 1.94 GHz, which is shown in Fig. 9.

In the second experiment, we measured the NEP as well as the optical efficiency for all KIDs, in an identical manner as in [13]. The definition and derivation of this optical efficiency for a multimode detector is provided in Appendix E. We first obtained the experimental NEP as a function of the source power

$$\mathrm{NEP}_{\mathrm{exp},P_s} = \sqrt{S_\theta} \left(\frac{\mathrm{d}\theta}{\mathrm{d}P_s} \right)^{-1}. \tag{3}$$

Here, S_θ is the KID phase noise, obtained from 128 s of time domain data taken at a constant radiator temperature, $\mathrm{d}\theta$ is the KID phase response to a change in the radiator power $\mathrm{d}P_s$. This was obtained by measuring the KID phase while performing a small temperature sweep of the radiator and performing a linear fit from the measured data. In all cases, P_s is calculated from the radiator temperature and the filter transmission as discussed in Appendix D.

In Fig. 12(b), we show the reduced frequency noise $S_x = S_\theta/(4Q_i)^2$ of KID 10 ($F_{\mathrm{res}} = 2.79$ GHz) for three different radiator temperatures. At modulation frequencies below 0.2 Hz, a multitone readout system is required to correct for the setup's drifts and reduce the noise spectra as discussed in [11]. The noise at $T_{\mathrm{BB}} = 12$ K, $P_{\mathrm{abs}} = 0.6$ aW, which represents still fully dark conditions, has a strong 1/f component. At the two higher black body temperatures, i.e., at absorbed powers above 65 aW [see more details in Fig. 19(b)], which are relevant for PRIMAger observation scenarios, the noise is white with a roll-off given by the quasiparticle lifetime. In this regime, the KIDs are photon noise limited [31], with a sensitivity dominated by the photon arrival rate fluctuations. Now we can use (26) in Appendix E to obtain the optical efficiency with respect to a single mode and one polarization η_{opt,f_0} from $\mathrm{NEP}_{\mathrm{exp},P_s}$, which is shown by the grey colored squares in Fig. 12(c). The inset indicates the optical efficiency found using this method. We obtain an average value of $\eta_{\mathrm{opt}} = 5.95$, which corresponds to receiving 5.95 times the power of a single mode at a single polarization. We repeat this procedure for all 23 KIDs and give the complete dataset in Fig. 13. We observe an optical efficiency that scatters between 4.3 and 5.95. The maximum coupling is in good agreement with the calculated value using the measured absorber geometry and Al resistivity, and corresponds to an aperture efficiency of 54%, as shown in Fig. 7(a). We attribute the scatter in efficiency to small lens-absorber misalignments due to a systematic shift between lens array and chip, which was caused by an $\approx 1.3^\circ$

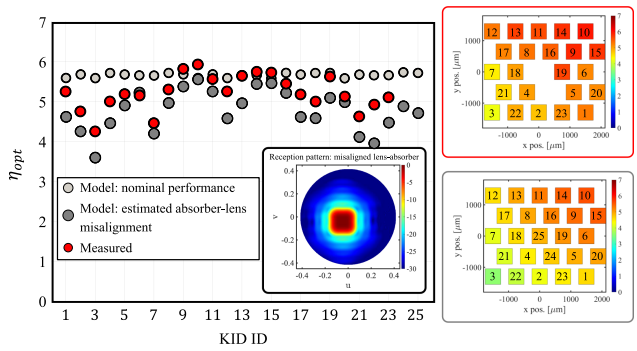

Fig. 13. Optical efficiency for all KIDs, the inner inset shows the power pattern of the lens absorber, at the centre of the array, when the absorber is laterally displaced with respect to the lens centre, which corresponds to the case of the assembled devices. The outer top and bottom insets indicate the spatial variation of the measured and modeled optical efficiency for each KID, respectively, where the KID's IDs are also provided.

off-vertical alignment between the chip plane and microscope z-axis used to align the lens array to the chip. We correct for this using an independent measurement of the coupling efficiency using a small aperture in our setup as discussed in Appendix F, and shown in Fig. 21. We find a misalignment of the lens array that can be described by a shift common to all detectors of $\simeq 29.9\hat{x} + 15.1\hat{y}$ μm with respect to a lens focal point, which is consistent with a separate measurement of the angle between the microscope z-axis and the chip plane. As a result, a corresponding beam tilt is present in the reception power pattern of the fabricated lens absorbers. The resulting tilted reception power pattern of the lens absorbers due to this misalignment is shown in the inset of Fig. 13, which repoints the beam maximum value (with respect to a lens optical axis) to 4.6° colatitude and 207° azimuth angles. Moreover, we expect slight rotation misalignment between the lens array and absorbers as well as slight misalignment variation for each of the 25 absorber-lenses. These higher order misalignment suspicions are not considered in the corrected model. Despite the described misalignment complications, we observe a good agreement between the measured and calculated results for both aperture sizes. It is noteworthy that the misalignment correction does not change the maximum coupling for the best detectors.

The agreement between measured and estimated optical efficiency implies that the experimental aperture efficiency of the lens-absorber is also in agreement with the one estimated by the model, i.e. $\eta_{\text{ap}}(6.98\ \text{THz}) = 0.54$ averaged over the two linear polarizations [see the grey coloured circle in Fig. 7(a)]. The reasoning for the validity of this indirect verification is as follows: the optical efficiency depends both on the reception power pattern (i.e., focusing efficiency) as well as the aperture efficiency, as described in Appendix D, (16). However, a negligible ambiguity is expected on the lens-absorber's reception power pattern. Two observations support this expectation: i) as shown in Fig. 14 in Appendix A, the reception power pattern depends strongly on the absorber total size and the lens diameter, but not the details of a unit cell nor the stratification. In the described prototype, the physical size of the absorbers and lens diameters are well controlled. ii) In the experiment with the smaller radiator aperture (see Fig. 21 in Appendix F), the optical efficiency depends strongly on the spillover efficiency of the setup [see (14)] and in turn to the reception power pattern of the lens absorber. In this case, the measured optical efficiency is still in fair agreement with the one from the model. Therefore, it is concluded that optical efficiency verification indirectly leads to an experimental validation of the aperture efficiency.

After obtaining the optical efficiency, we can obtain $\text{NEP}_{\text{exp},P_{\text{abs}}}$, which is shown in Fig. 12(c) for KID 10 using (24) in Appendix D. We reach a limiting NEP of $\text{NEP}_{\text{exp},P_{\text{abs}}} = 8 \cdot 10^{-20}$ $\text{W}/\sqrt{\text{Hz}}$ at a modulation frequency, F_{mod}, of 100 Hz, which increases at lower modulation frequencies due to the 1/f noise. This result is typical for all devices, as shown in Fig. 20 in Appendix F. We also refer to Appendix F for the noise and NEP data at wider range of radiator temperatures (see Fig. 19), to illustrate the radiation power dependence of the NEP and the noise of the detectors presented in this work. This noise transforms from an 1/f spectrum at low absorbed powers to a white spectrum for $P_{\text{abs}} > 69$ fW. It is interesting to compare these results to recent work from Day et al. [14], which discusses a similar detector but optimized for higher frequencies. These devices have a lower NEP than the devices presented here, especially at low modulation frequencies. Moreover, in this work, we have observed a shorter average maximum quasiparticle recombination time of 0.5 ms obtained using a single Lorentzian fit to the noise cross power spectral density. This can possibly be attributed to one or more of the following reasons:

1) differences in the fabrication methodology;
2) the absorber volume, which is 4 folds larger in our devices; and
3) the fact that the quasiparticle density at low temperature and negligible power case can be limited by the readout power, which is both absorber volume and readout frequency dependent [42].

V. Conclusion

In this article, a detector concept based on lens absorber coupled KIDs is proposed to address the requirements of future space-based FIR astronomical instruments in terms background limited sensitivity and FPA scalability. The EM coupling of the detectors placed below focusing lens components is modeled via a spectral technique developed in previous contributions. This technique provided an accurate and numerically efficient manner to describe the relevant figures of merit, design guidelines, and tolerance studies for lens absorbers. Two dual polarized lens absorber couple KIDs operating at central frequencies of 6.98 and 12 THz, relevant to PRIMAger bands, were presented. The design for 6.98 THz was fabricated as a hexagonal array of 25 detectors with a yield of 92%. The performance of the prototype array in terms of optical coupling was experimentally validated against the one estimated by the model with good agreement. This also indirectly validated the aperture efficiency of the lens absorbers against the expected value of $\simeq 54\%$. The NEP of the absorber-based KIDs was also quantified with a minimum achieved value of 8×10^{-20} $\text{W}/\sqrt{\text{Hz}}$ satisfying the targeted sensitivity requirements. The experimental verifications

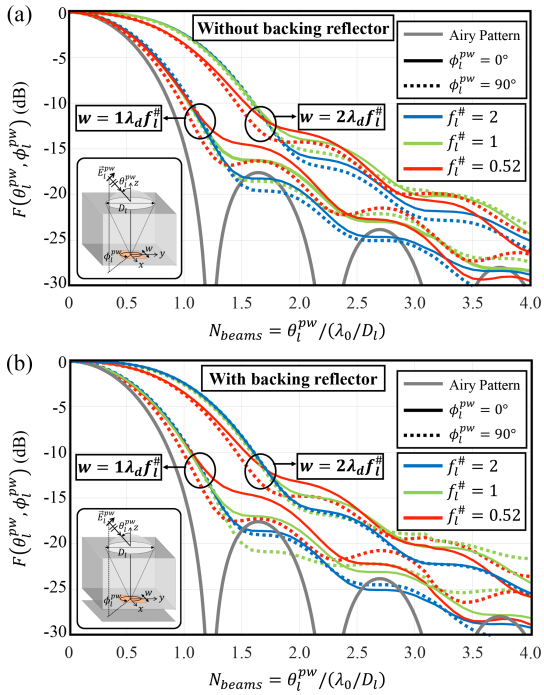

Fig. 14. Normalized reception power pattern for two absorber sampling rates and three lens f-number cases: ideal absorber (a) without and (b) with quarter wavelength backing reflector. The insets indicates the scenarios under consideration. The incident plane wave illuminating the lenses is y-polarized.

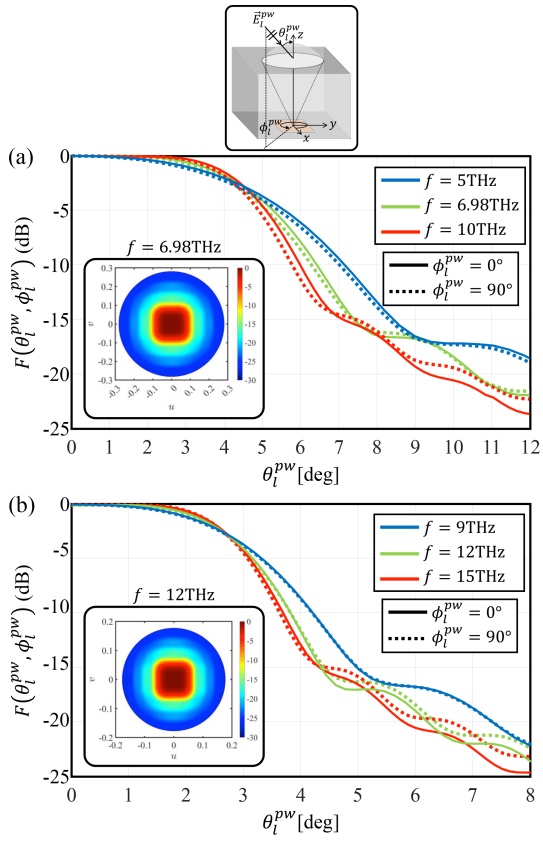

Fig. 15. Reception power pattern of the designed (a) 6.98 and (b) 12 THz lens absorbers against the incident angle of the plane wave illuminating the lens for the lower, centre, and higher frequency points of their operation band. The patterns are the averaged response of the detectors to a combination of the two linear polarizations.

shown in this work indicate that the design, fabrication, and performance of the proposed lens absorber coupled KIDs is well understood providing confidence in developing flight detectors for space-based FIR astronomical instruments, and in particular PRIMA.

Appendix A
EM Figures of Merit for a Lens Absorber

In this Appendix, the figures of merit, derived in [19] for bare absorbers below reflectors, for describing the EM performance of a lens absorber are reviewed.

Aperture efficiency, η_{ap}, indicates how much of the incident point source power is captured by the absorber [19]

$$\eta_{\text{ap}}(f) = \frac{\max\{P_{\text{abs}}(f, \theta_l^{\text{pw}}, \phi_l^{\text{pw}})\}}{P_{\text{inc}}} \tag{4}$$

where $P_{\text{inc}} = 1/(2\zeta_0)|E_0^{\text{pw}}|^2 A_{\text{lens}}$ is the power illuminating the lens surface via an incident plane wave, ζ_0 is the characteristic impedance in free space, E_0^{pw} is the amplitude of the incident plane wave, and A_{lens} is the area of the lens aperture.

Reception power pattern of the lens absorber, indicates its normalized angular response to point sources [19]

$$F(f, \theta_l^{\text{pw}}, \phi_l^{\text{pw}}) = \frac{P_{\text{abs}}(f, \theta_l^{\text{pw}}, \phi_l^{\text{pw}})}{\max\{P_{\text{abs}}(f, \theta_l^{\text{pw}}, \phi_l^{\text{pw}})\}}. \tag{5}$$

The normalized reception power pattern for two absorber sampling sizes and the two ideal absorbers, described in Section II-B, is shown in Fig. 14 and compared to the diffraction limited case, i.e., to their corresponding Airy patterns.

Focusing efficiency compares the angular selectivity of the lens absorber against the diffraction limit [19]

$$\eta_f(f) = \frac{\lambda_0^2/A_{\text{lens}}}{\int_0^{2\pi}\int_0^{\pi/2} F(f, \theta_l^{\text{pw}}, \phi_l^{\text{pw}}) \sin\theta_l^{\text{pw}} \mathrm{d}\theta_l^{\text{pw}} \mathrm{d}\phi_l^{\text{pw}}} \tag{6}$$

where λ_0 is the free-space wavelength at frequency f; the numerator and the denominator are the solid angles in diffraction limit [43], and the one of the lens absorber, respectively.

Appendix B
Additional EM Results for the Designed Lens Absorbers

In this Appendix, additional results related to the designed lens absorbers operating at the central frequencies of 6.98 and 12 THz are reported.

Lens absorbers performance in terms of the reception power pattern over their operation frequency bands is shown in Fig. 15.

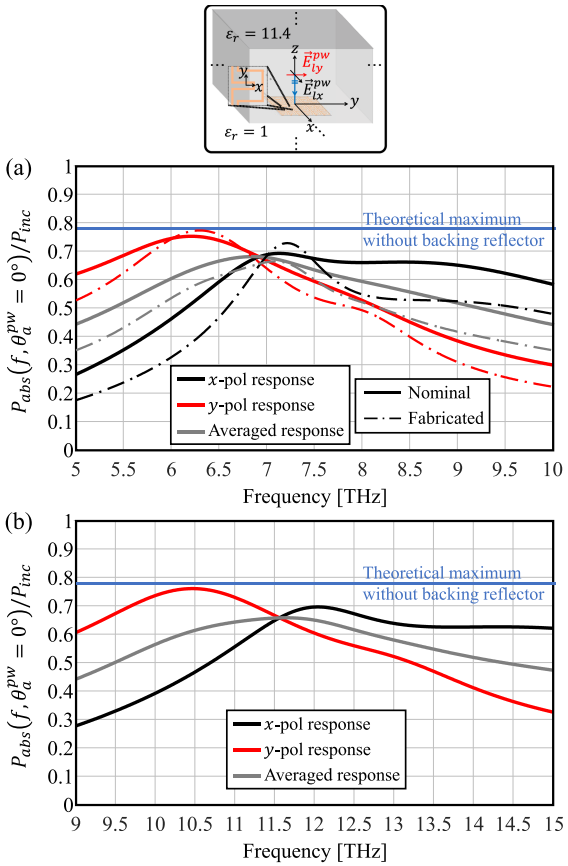

Fig. 16. Broadside plane wave response of (a) 6.98 THz absorber and (b) 12 THz absorber as a function of operation frequency. The insets indicate the orientation of the unit cells with respect to x- and y-polarized plane waves. The solid and dotted lines correspond to the designed and fabricated devices, respectively. The blue solid lines indicate the theoretical maximum value based on Fig. 3.

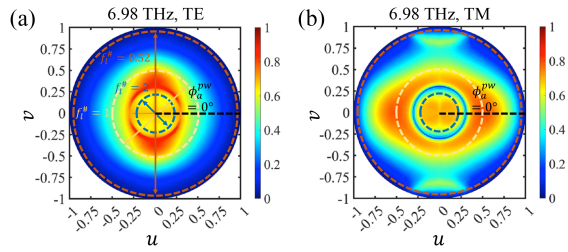

Fig. 17. (a) TE and (b) TM polarized plane wave responses of 6.98 THz absorber projected into u–v coordinates, where $u = \sin\theta_a^{\text{pw}} \cos\phi_a^{\text{pw}}$ and $v = \sin\theta_a^{\text{pw}} \sin\phi_a^{\text{pw}}$. The indicated angular regions correspond to the three considered lens f-number cases, and data of the indicated cut is shown in Fig. 6.

These power patterns are symmetric over the azimuth direction with expected frequency variations due to the size of the absorbers in terms of wavelength. The spectral response of the absorbers to broadside TE and TM plane wave incidents in Si as a function of operation frequency is shown in Fig. 16 while the 2-D spectral response of the 6.98 THz absorber as a function of incident angles at the central frequency is shown in Fig. 17.

Appendix C
Calculation of the Characteristic Impedance of a NbTiN CPW Line

The characteristic impedance of the NbTiN CPW line, $Z_{\text{eff, NbTiN}} = \sqrt{L_{\text{tot}}/C_{\text{geo}}}$, can be calculated by including the NbTiN kinetic inductance L_k at the readout frequency F in the total inductance, $L_{\text{tot}} = L_{\text{geo}} + L_k$, where L_{geo} is the geometric inductance. The sheet kinetic inductance L_s can be calculated at $hF, k_BT \ll 2\Delta$ using [37]

$$L_s = \frac{hR_s}{\pi\Delta} \tag{7}$$

with R_s the NbTiN sheet resistance, $\Delta = 1.76 \cdot k_BT_c$ the superconducting energy gap. The kinetic inductance per unit length of the CPW line can then be obtained by following Collin et al. [44]:

$$L_k = L_s \cdot (g_g + g_c) \quad \text{with} \tag{8}$$

$$g_c(S, W) = \frac{1}{4S(1-k^2)K^2(k)} \left[\pi + \ln\left(\frac{4\pi S}{d}\right) - k\ln\left(\frac{1+k}{1-k}\right)\right] \tag{9}$$

$$g_g(S, W) = \frac{k}{4S(1-k^2)K^2(k)} \left[\pi + \ln\left(\frac{4\pi(S+2W)}{d}\right) - \frac{1}{k}\ln\left(\frac{1+k}{1-k}\right)\right] \tag{10}$$

$$\text{with } k = \frac{S}{S+2W}. \tag{11}$$

Here S, W are the NbTiN CPW line and gap widths, respectively, d is the metal thickness and K is the complete elliptical integral of the first kind. The phase velocity can now be calculated using the standard expression $v_p = \sqrt{1/(L_{\text{tot}}C_{\text{geo}})}$.

Appendix D
Experimental Setup

We give a cross section of the experimental setup in Fig. 18. It is conceptually similar to the one originally presented in [40] and used also in [13]. We use a box-in-box at 130 mK consisting of a light tight box, with all metal slits equipped with stray light labyrinths and their interior coated over by large area absorbers. The absorber material is Epotek920 epoxy with 3% by weight carbon black with SiC grains. We first apply a thin layer of epoxy, then sprinkle the SiC grains, shake off the loose grains and bake out at 90 °C for half an hour. After that we cover this layer with a thin layer of the Epotek/carbon mix, making sure the surface roughness is maintained. For large areas, we use 1 mm SiC grains, for the labyrinths we use 0.2 mm SiC grains. We modified the setup with respect to recent work in [45] with respect to the clamping of the filters: every filter clamp is now carefully equipped with radiation absorbers, and we added a second filter stage on the light tight box. Both additions were needed to prevent any detector response below a radiator temperature of 12 K, where the in-band power is $\approx 10^{-21}$ W, corresponding

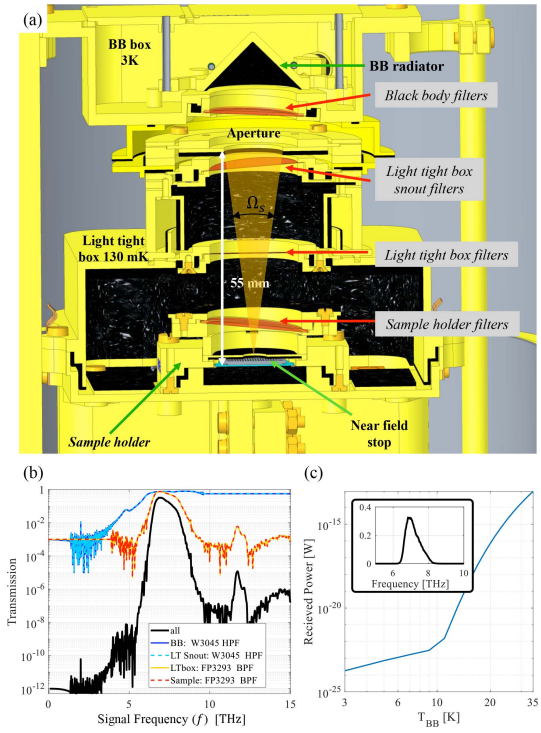

Fig. 18. (a) Cross sectional view of the experimental setup. (b) Transmissions of the individual filters in the setup, together with the total transmission. (c) Source power as function of radiator temperature for a single mode (and one polarization). The inset shows the total filter transmission, same as in panel (b), but in a linear scale.

to a photon rate of around $0.1/\text{sec}$. Note that all filter stages in Fig. 18(a) are slightly angled to prevent standing waves. In Fig. 18(b), we show the filters used: HPFs at the radiator and snout position, and BPFs at the light tight box and sample holder. The low-frequency rejection is about -120 dB, even so the source power is dominated by long wavelength radiation for radiator temperatures below 11 K, which can be seen in panel (c) of the figure. We decided not to increase the amount of filters as the power transmitted is below 10^{-22} W, well below our detector detection threshold.

Appendix E
Definition of Optical Efficiency in Multimode Detectors and Its Estimation From Measured NEP

In order to evaluate the optical coupling of a multimode detector system, the power absorbed by a detector in a measurement setup is characterized here. The power absorbed by the detectors when illuminated by the setup's black body radiator, modeled as an incoherent distributed source, is estimated as

$$P_{\text{abs}} = \int_{f_1}^{f_2} \iint_{\Omega_s} B_s(f) A_{\text{eff}}\left(f, \theta_l^{\text{pw}}, \phi_l^{\text{pw}}\right) F_{il}(f) \mathrm{d}f \mathrm{d}\Omega \quad (12)$$

where f is the frequency of the arriving photons, $B_s(f)$ is the brightness of the distributed source, $F_{il}(f)$ is the response of the filter stages within the measurement setup; f_1 and f_2 are the lower and higher ends of the operation bandwidth, $\mathrm{d}\Omega = \sin\theta_l^{\text{pw}} \mathrm{d}\theta_l^{\text{pw}} \mathrm{d}\phi_l^{\text{pw}}$ and Ω_s is the solid angle of the source seen by the detector [see Fig. 18(a)]. $A_{\text{eff}}(f, \theta_l^{\text{pw}}, \phi_l^{\text{pw}})$ is the effective area of the detector

$$A_{\text{eff}}(f, \theta_l^{\text{pw}}, \phi_l^{\text{pw}}) = A_{\text{lens}} \left[\frac{1}{2}\eta_{\text{ap}}^{\text{pol-1}}(f) F^{\text{pol-1}}\left(f, \theta_l^{\text{pw}}, \phi_l^{\text{pw}}\right) + \frac{1}{2}\eta_{\text{ap}}^{\text{pol-2}}(f) F^{\text{pol-2}}\left(f, \theta_l^{\text{pw}}, \phi_l^{\text{pw}}\right)\right] \quad (13)$$

where A_{lens} is the area of the lens aperture, $\eta_{\text{ap}}^{\text{pol-1}}$ and $\eta_{ap}^{\text{pol-2}}$ are the aperture efficiencies of the detector for linear polarizations 1 and 2, respectively; and $F^{\text{pol-1}}(f, \theta_l^{\text{pw}}, \phi_l^{\text{pw}})$ and $F^{\text{pol-2}}(f, \theta_l^{\text{pw}}, \phi_l^{\text{pw}})$ are their normalized reception power patterns.

The spill over efficiency within the measurement setup can be estimated as

$$\eta_{so}^{\Omega_s, \text{pol-}i}(f) = \frac{\iint_{\Omega_s} F^{\text{pol-}i}(f, \theta_l^{\text{pw}}, \phi_l^{\text{pw}}) \mathrm{d}\Omega}{\iint_{2\pi} F^{\text{pol-}i}(f, \theta_l^{\text{pw}}, \phi_l^{\text{pw}}) \mathrm{d}\Omega} \quad (14)$$

where the superscript pol-i represents the corresponding values for polarization $i = 1$ or 2.

By using (6) and (14), the power absorbed from a distributed source can be rewritten as

$$P_{\text{abs}} = \int_{f_1}^{f_2} \frac{1}{2}\lambda_0^2 B_s(f) F_{il}(f) \eta_{\text{so}}^{\Omega_s, \text{pol-1}}(f) \frac{\eta_{\text{ap}}^{\text{pol-1}}(f)}{\eta_f^{\text{pol-1}}(f)} \mathrm{d}f + \int_{f_1}^{f_2} \frac{1}{2}\lambda_0^2 B_s(f) F_{il}(f) \eta_{\text{so}}^{\Omega_s, \text{pol-2}}(f) \frac{\eta_{\text{ap}}^{\text{pol-2}}(f)}{\eta_f^{\text{pol-2}}(f)} \mathrm{d}f \quad (15)$$

where the power absorbed from each polarization is separated explicitly. The optical efficiency (also referred to as the normalized throughput in the literature [26], [19]) for a multimode detector for each polarization is then expressed as

$$\eta_{\text{opt}}^{\text{pol-}i}(f) = \frac{\eta_{\text{so}}^{\Omega_s, \text{pol-}i}(f) \eta_{ap}^{\text{pol-}i}(f)}{\eta_f^{\text{pol-}i}(f)}. \quad (16)$$

Using this definition, (15) is rearranged for each polarization as

$$P_{\text{abs}}^{\text{pol-}i} = \int_{f_1}^{f_2} \eta_{\text{opt}}^{\text{pol-}i}(f) P_{\text{sf}}(f) \mathrm{d}f \quad (17)$$

where

$$P_{\text{sf}}(f) = \frac{1}{2}\lambda_0^2 B_s(f) F_{il}(f) \quad (18)$$

is the black body power transmitted per frequency and per polarization, which can couple to a single mode detector.

The photon noise limited NEP of a KID is given by [13]

$$\text{NEP}_{\text{tot}}^2 = \text{NEP}_{\text{Poisson}}^2 + \text{NEP}_{\text{Wave}}^2 + \text{NEP}_{qp}^2. \quad (19)$$

We need to evaluate these terms at the detector, i.e., with respect to absorbed power, as the bunching term, NEP_{Wave}, is determined by the absorption process. The first righthand side term in (19), $\text{NEP}_{\text{Poisson}}$, is the Poisson noise due to random photon fluctuations, which is the dominating term in the Wien's limit. This term is expressed using (17) and [46] as

$$\text{NEP}_{\text{Poisson}}^2(P_{\text{abs}}^{\text{pol-}i}) = \int_{f_1}^{f_2} 2\eta_{\text{opt}}^{\text{pol-}i}(f) P_{\text{sf}}(f) h f \mathrm{d}f. \quad (20)$$

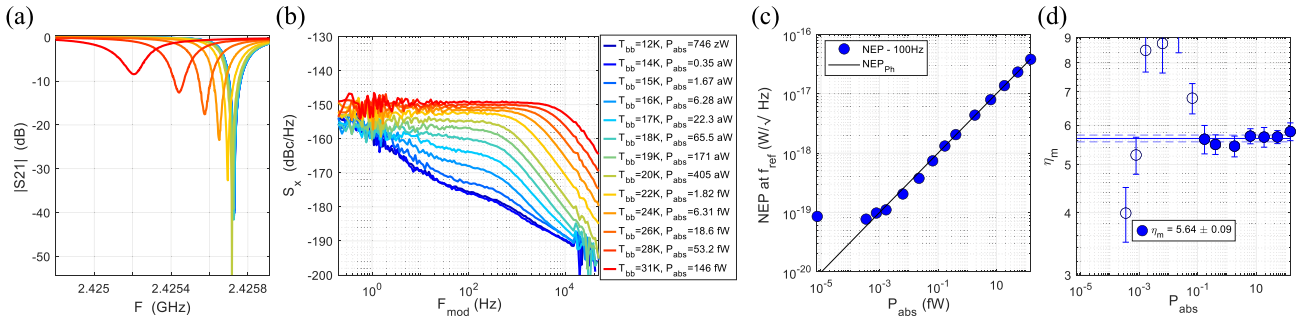

Fig. 19. Results of an experiment with 12 radiator temperatures for KID 9 with $F_{\text{res}} = 2.43$ GHz. (a) Forward transmission for all measured radiator temperatures, clearly showing the KID dip reducing and moving to lower frequencies. (b) Reduced frequency noise spectra, where we clearly observe the transition from a (partial) detector $1/f$ noise limited NEP to a white, photon noise limited NEP for $P_{\text{abs}} > 65.5$ fW. (c) NEP as function of absorbed power at a modulation frequency of $F_{\text{mod}} = 100$ Hz. (d) Corresponding optical efficiency obtained from NEP values in (c).

The second right-hand side term in (19), NEP_{Wave}, is the wave bunching term, which dominates the noise in Rayleigh–Jeans's limit. This term is expressed using (15) and [46] as

$$\text{NEP}^2_{\text{Wave}}\left(P^{\text{pol-}i}_{\text{abs}}\right) = \int_{f_1}^{f_2} 2\left(\eta^{\text{pol-}i}_{\text{opt}}(f)\right)^2 P_{sf}(f) h f F_{il}(f) O_f(f) \mathrm{d}f \quad (21)$$

where $O_f(f) = (e^{hf/(k_B T)} - 1)^{-1}$ is the photon occupation number per mode, and T is the temperature of the radiator.

The final right-hand side term in (19), NEP_{qp}, is the noise added due to random recombination of quasi-particles in a KID. This term is expressed using (15) and [46] as

$$\text{NEP}^2_{qp}\left(P^{\text{pol-}i}_{\text{abs}}\right) = \int_{f_1}^{f_2} 4\eta^{\text{pol-}i}_{opt}(f) \Delta P_{\text{sf}}(f)/\eta_{qp} \mathrm{d}f \quad (22)$$

where η_{qp} is the quasi-particle creation efficiency.

In the limit of small operational bandwidth around a central frequency f_0 defined by a set of quasi-optical filters the absorbed power can be expressed by using (17) as

$$P^{\text{pol-}i}_{\text{abs}} = \eta_{\text{opt},f_0} \int_{f_1}^{f_2} P_{\text{sf}}(f) \mathrm{d}f \quad (23)$$

where η_{opt,f_0} is the coupling efficiency at f_0 with respect to a single mode and a single polarization.

The total photon noise limited NEP of the MKID as a function of the power absorbed can now be readily obtained by substituting (20), (21) and (22) in (19)

$$\begin{aligned}\text{NEP}^2_{\text{Ph},P_{\text{abs}}} &= \eta_{\text{opt},f_0} \int_{f_1}^{f_2} 2P_{\text{sf}}(f) h f \mathrm{d}f \\ &+ \eta^2_{\text{opt},f_0} \int_{f_1}^{f_2} 2P_{\text{sf}}(f) h f F_{il}(f) O_f(f) \\ &+ \eta_{\text{opt},f_0} \int_{f_1}^{f_2} 4\Delta P_{\text{sf}}(f)/\eta_{qp} \mathrm{d}f. \end{aligned} \quad (24)$$

In an analogous way we can substitute (23) in (3) to relate the experimental NEP as a function of source and absorbed power to each other

$$\text{NEP}^2_{\text{exp},P_{\text{abs}}} = S_x \left(\frac{dx}{\mathrm{d}P_{\text{abs}}}\right)^{-2} = \eta^2_{\text{opt}} \text{NEP}^2_{\text{exp},P_s}. \quad (25)$$

In our experiment, we measure first the detector NEP as function of the source power available in front of the detector (3), which depends on the black body temperature and filters used in the experiment. To evaluate the NEP at the detector we need to obtain the optical efficiency $\eta_{\text{opt}}(f_0)$. This can be achieved in the limit that the detector NEP is photon noise limited. Following Janssen et al. [31], this is the case when the KID noise power spectral density is white with a roll-off given by the quasiparticle lifetime. In our experiment, this is the case for black body temperatures equal to and exceeding 18 K, as can be seen from Fig. 19. In these cases $\text{NEP}_{\text{Ph},P_{\text{abs}}} = \text{NEP}_{\text{exp},P_{\text{abs}}}$ and we can use (24) and (25) to obtain the optical efficiency with respect to a single mode and a single polarization

$$\eta_{\text{opt},f_0} = \frac{\int_{f_1}^{f_2} 2P_{\text{sf}}(f) h f \mathrm{d}f + \int_{f_1}^{f_2} 4\Delta P_{\text{sf}}(f)/\eta_{qp} \mathrm{d}f}{\text{NEP}^2_{\text{exp},P_s} - \int_{f_1}^{f_2} 2P_{\text{sf}}(f) h f F_{il}(f) O_f(f)} \quad (26)$$

which can be evaluated experimentally as all its terms are known.

For a dual polarized detector (23) is valid when

$$\eta_{\text{opt},f_0} = \eta^{\text{pol-1}}_{\text{opt}}(f_0) + \eta^{\text{pol-2}}_{\text{opt}}(f_0). \quad (27)$$

In this work, the results shown for the optical efficiency compare the measured response using (26) against the ones estimated by the model using (27) and (16).

Appendix F
Additional Experimental Results

To get more insight in the radiation power dependence of the KID noise and NEP, we measured for two KIDs the NEP for 12 radiator temperatures, the (representative) result for KID 9 is shown in Fig. 19. In panel (a), we show the KID resonance features, where we clearly see the expected frequency shift and depth decrease with increasing absorbed power. Interestingly at a radiator temperature of 31 K, corresponding to $P_{\text{abs}} = 151$ fW we still observe an 8 dB deep resonance with an estimated internal quality factor of $\simeq 22 \times 10^3$, indicating that this KID works well at power levels exceeding 151 fW. In panels (b) and (c), we show the noise and NEP, respectively. It is clear that the

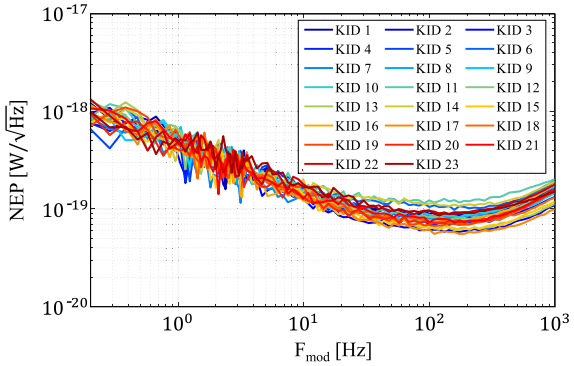

Fig. 20. NEP spectra for all KIDs at negligible radiation load and at 130 mK.

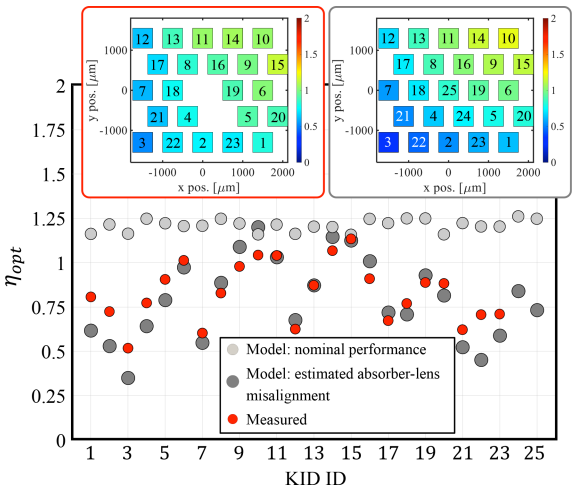

Fig. 21. Optical efficiency for all KIDs when the diameter of the aperture is reduced from 15 mm (case in Fig. 13) to 4.5 mm. The left and right-hand side insets show the spatial dependency of the optical efficiency for each KID from the measured and modeled data, respectively, where the KID's IDs are also provided.

device moves from partly 1/f noise limited to background limited performance, with a white noise down to 0.1 Hz, for radiator temperatures exceeding 18 K, corresponding to $P_{\text{abs}} = 65$ aW.

In Fig. 19(c), we give the NEP at 100 Hz modulation frequency, which shows clearly how the NEP follows the expected square root power dependence for background limited operation down to $P_{\text{abs}} \approx 1$ aW, indicating the superior performance at higher modulation frequencies. The inset shows the measured optical efficiency for each radiation power. To calculate the efficiency we only use the data with power levels exceeding 0.1 fW where, at 100 Hz, the device is background limited. The KIDs in this chip all show a very similar NEP under dark conditions and at 130 mK, this is shown in Fig. 20.

In Fig. 21, the optical efficiencies are shown for all 23 KIDs, which are obtained experimentally when the diameter of the aperture between the black body radiator and the lens array is reduced from 15 to 4.5 mm with respect to the data provided in Fig. 13 (corresponding to a full width opening angle of $4.8°$). The nominal and misaligned theoretical values of the optical efficiency are also calculated and compared against experimental ones showing a very good agreement.

REFERENCES

[1] H. Dole et al., "The cosmic infrared background resolved by spitzer. contributions of mid-infrared galaxies to the far-infrared background," *Astron. Astrophys.*, vol. 451, pp. 417–429, May 2006.

[2] D. Farrah et al., "Review: Far-infrared instrumentation and technological development for the next decade," *J. Astron. Telescopes, Instruments, Syst.*, vol. 5, Apr. 2019, Art. no. 020901.

[3] J. Glenn et al., "Prima: The probe far-infrared mission for astrophysics," *SPIE Astron. Telescopes Instrum.*, vol. 13092, Aug. 2024, Art. no. 130920J, doi: 10.1117/12.3017620.

[4] J. Glenn and et al., "PRIMA mission concept," *J. Astron. Telescopes, Instruments, Syst.*, vol. 11, no. 3, 2025, Art. no. 031628, doi: 10.1117/1.JATIS.11.3.031628.

[5] L. Ciesla et al., "PRIMA: PRIMAger, a far infrared hyperspectral and polarimetric instrument," vol. 13092, 2024, Art. no. 130920K, doi: 10.1117/12.3018739.

[6] K. M. Pontoppidan et al., "The far-infrared enhanced survey spectrometer (firess) for prima: Science drivers," 2025. [Online]. Available: https://arxiv.org/abs/2509.01800

[7] K. Irwin and G. Hilton, *Transition-Edge Sensors*. Berlin Germany, Springer Jul. 2005, pp. 63–150, doi: 10.1007/10933596_3.

[8] P. C. Nagler, J. E. Sadleir, and E. J. Wollack, "Demonstration of ultra-low noise equivalent power using a longitudinal proximity effect transition-edge sensor," 2020, *arXiv:2012.06543*.

[9] P. M. Echternach, A. D. Beyer, and C. M. Bradford, "Large array of low-frequency readout quantum capacitance detectors," *J. Astron. Telescopes, Instruments, Syst.*, vol. 7, no. 1, pp. 1–8, 2021, doi: 10.1117/1.JATIS.7.1.011003.

[10] P. K. Day, H. G. LeDuc, B. A. Mazin, A. Vayonakis, and J. Zmuidzinas, "A broadband superconducting detector suitable for use in large arrays," *Nature*, vol. 425, 2003, Art. no. 817.

[11] J. J. A. Baselmans et al., "A kilo-pixel imaging system for future space based far-infrared observatories using microwave kinetic inductance detectors," *Astron. Astrophys.*, vol. 601, May 2017, Art. no. A89.

[12] J. Bueno, V. Murugesan, K. Karatsu, D. J. Thoen, and J. J. A. Baselmans, "Ultrasensitive kilo-pixel imaging array of photon noise-limited kinetic inductance detectors over an octave of bandwidth for THz astronomy," *J. Low Temp. Phys.*, vol. 193, no. 3/4, pp. 96–102, Nov. 2018.

[13] J. J. A. Baselmans et al., "Ultra-sensitive THz microwave kinetic inductance detectors for future space telescopes," *Astron. Astrophys.*, vol. 665, Sep. 2022, Art. no. A17.

[14] P. K. Day et al., "A 25-micrometer single-photon-sensitive kinetic inductance detector," *Phys. Rev. X*, vol. 14, no. 4, Oct. 2024, Art. no. 041005.

[15] S. Masi et al., "Kinetic inductance detectors for the OLIMPO experiment: In-flight operation and performance," *J. Cosmol. Astroparticle Phys.*, vol. 2019, no. 7, Jul. 2019, Art. no. 003.

[16] S. Hailey-Dunsheath et al., "Development of aluminum LEKIDs for balloon-borne far-IR spectroscopy," *J. Low Temp. Phys.*, vol. 193, no. 5/6, pp. 968–975, Dec. 2018.

[17] K. Karatsu et al., "Mitigation of cosmic ray effect on microwave kinetic inductance detector arrays," *Appl. Phys. Lett.*, vol. 114, no. 3, Jan. 2019, Art. no. 032601.

[18] K. Karatsu et al., "Radiation tolerance of aluminum microwave kinetic inductance detector," *J. Low Temp. Phys.*, vol. 184, pp. 540–546, Aug. 2016.

[19] N. Llombart, S. O. Dabironezare, G. Carluccio, A. Freni, and A. Neto, "Reception power pattern of distributed absorbers in focal plane arrays: A Fourier optics analysis," *IEEE Trans. Antennas Propag.*, vol. 66, no. 11, pp. 5990–6002, Nov. 2018, doi: 10.1109/TAP.2018.2862359.

[20] M. Calvo et al., "The NIKA2 instrument, a dual-band kilopixel KID array for millimetric astronomy," *J. Low Temp. Phys.*, vol. 184, no. 3/4, pp. 816–823, Mar. 2016, doi: 10.1007/s10909-016-1582-0.

[21] P. S. Barry et al., "Design and performance of the antenna-coupled lumped-element kinetic inductance detector," *J. Low Temp. Phys.*, vol. 193, pp. 176–183, Nov. 2018.

[22] N. Llombart, B. Blazquez, A. Freni, and A. Neto, "Fourier optics for the analysis of distributed absorbers under thz focusing systems," *IEEE Trans. THz Sci. Technol.*, vol. 5, no. 4, pp. 573–583, Jul. 2015, doi: 10.1109/TTHZ.2015.2439511.

[23] S. O. Dabironezare et al., "A dual-band focal plane array of kinetic inductance bolometers based on frequency-selective absorbers," *IEEE Trans. THz Sci. Technol.*, vol. 8, no. 6, pp. 746–756, Nov. 2018, doi: 10.1109/TTHZ.2018.2873973.

[24] S. O. Dabironezare, G. Carluccio, A. Freni, A. Neto, and N. Llombart, "Coherent Fourier optics model for the synthesis of large format lens-based focal plane arrays," *IEEE Trans. Antennas Propag.*, vol. 69, no. 2, pp. 734–746, Feb. 2021, doi: 10.1109/TAP.2020.3016501.
[25] S. van Berkel et al., "Relative observing speed of lens-coupled absorber focal plane arrays for far-IR imaging and spectroscopy: A PRIMA case study," *J. Astron. Telescopes, Instruments, Syst.*, vol. 11, May 2025, Art. no. 031613, doi: 10.1117/1.JATIS.11.3.031613.
[26] M. J. Griffin, J. J. Bock, and W. K. Gear, "Relative performance of filled and feedhorn-coupled focal-plane architectures," *Appl. Opt.*, vol. 41, no. 31, pp. 6543–6554, Nov. 2002. [Online]. Available: https://opg.optica.org/ao/abstract.cfm?URI=ao-41-31-6543
[27] B. Blazquez, N. Llombart, D. Cavallo, A. Freni, and A. Neto, "A rigorous equivalent network for linearly polarized thz absorbers," *IEEE Trans. Antennas Propag.*, vol. 62, no. 10, pp. 5077–5088, Oct. 2014, doi: 10.1109/TAP.2014.2341292.
[28] CST, "Cst microwave studio." Accessed: Sep. 24, 2025. [Online]. Available: http://www.cst.com
[29] R. Matick, *Transmission Lines for Digital and Communication Networks*. London, U.K.: IEEE Press, 1995.
[30] C. Molero, M. Garcia-Vigueras, R. Rodriguez-Berral, F. Mesa, and N. Llombart, "Equivalent circuit approach for practical applications of meander-line gratings," *IEEE Antennas Wireless Propag. Lett.*, vol. 16, pp. 3088–3091, 2017, doi: 10.1109/LAWP.2017.2756438.
[31] R. M. J. Janssen et al., "High optical efficiency and photon noise limited sensitivity of microwave kinetic inductance detectors using phase readout," *Appl. Phys. Lett.*, vol. 103, no. 20, 2013, Art. no. 203503. [Online]. Available: http://scitation.aip.org/content/aip/journal/apl/103/20/10.1063/1.4829657
[32] J. Gao, J. Zmuidzinas, B. A. Mazin, H. G. LeDuc, and P. K. Day, "Noise properties of superconducting coplanar waveguide microwave resonators," *Appl. Phys. Lett.*, vol. 90, 2007, Art. no. 102507.
[33] Sonnet software, Sonnet. Accessed: Sep. 24, 2025. [Online]. Available: https://www.sonnetsoftware.com/
[34] S. J. C. Yates et al., "Surface wave control for large arrays of microwave kinetic inductance detectors," *IEEE Trans. THz Sci. Technol.*, vol. 7, no. 6, pp. 789–799, Nov. 2017.
[35] D. J. Thoen et al., "Superconducting NbTiN thin films with highly uniform properties over a 100 mm ∅ wafer," *IEEE Trans. Appl. Supercond.*, vol. 27, no. 4, Jun. 2017, Art. no. 2631948.
[36] S. J. C. Yates et al., "Clean beam patterns with low crosstalk using 850 GHz microwave kinetic inductance detectors," *J. Low Temp. Phys.*, vol. 176, pp. 761–766, Sep. 2014.
[37] H. G. Leduc et al., "Titanium nitride films for ultrasensitive microresonator detectors," *Appl. Phys. Lett.*, vol. 97, 2010, Art. no. 102509.
[38] Veldlaser. Accessed: Sep. 24, 2025. [Online]. Available: https://www.veldlaser.nl/
[39] M. Ji, C. Musante, S. Yngvesson, A. J. Gatesman, and J. Waldman, "Study of parylene as anti-reflection coating for silicon optics at thz frequencies," in *Proc. 11th Int. Symp. Space Terahertz Technol.*, Ann Arbor, MI, USA, 2000, pp. p398–406.
[40] J. Baselmans, S. Yates, P. Diener, and P. de Visser, "Ultra low background cryogenic test facility for far-infrared radiation detectors," *J. Low Temp. Phys.*, vol. 167, pp. 360–366, 2012.
[41] S. Shu et al., "Increased multiplexing of superconducting microresonator arrays by post-characterization adaptation of the on-chip capacitors," *Appl. Phys. Lett.*, vol. 113, no. 8, Aug. 2018, Art. no. 082603, doi: 10.1063/1.5040968.
[42] S. A. H. de Rooij et al., "Volume dependence of microwave induced excess quasiparticles in superconducting resonators," 2025. [Online]. Available: https://arxiv.org/abs/2503.07443
[43] J. W. Goodman, *Statistical Optics*, 2nd ed. Hoboken, NJ, USA: Wiley, 2015, Art. no. 211.
[44] R. Collin, *Foundations for Microwave Engineering*, 2nd ed. New York, NY, USA: McGraw-Hill College, 1992.
[45] J. J. A. Baselmans and S. J. C. Yates, "Long quasiparticle lifetime in aluminium microwave kinetic inductance detectors using coaxial stray light filters," *AIP Conf. Proc.*, vol. 1185, pp. 160–163, 2009.
[46] L. Ferrari et al., "Antenna coupled MKID performance verification at 850GHz for large format astrophysics arrays," *IEEE Trans. THz Sci. Technol.*, vol. 8, no. 1, pp. 127–139, Jan. 2018.

Shahab Oddin Dabironezare (Member, IEEE) was born in Mashhad, Iran. He received the B.Sc. degree (*cum laude*) in electrical engineering-communications from the Ferdowsi University of Mashhad (FUM), Mashhad, Iran, in 2013, and the M.Sc. and Ph.D. degrees in electrical engineering from the Delft University of Technology (TU Delft), Delft, The Netherlands, in 2015 and 2020, respectively.

From 2020 to 2022, he was a Postdoctoral Researcher with the Department of Microelectronics, Terahertz (THz) Sensing Group, TU Delft. He is currently an Assistant Professor with the THz Sensing Group, TU Delft, and an Instrument Scientist with the Space Research Organisation Netherlands (SRON), Leiden, The Netherlands. His research interests include wide-band antennas at millimetre and submillimetre wave applications, lens absorbers and antennas for far-infra red astronomy, and wide field-of-view quasi-optical systems.

Giulia Conenna, photograph and biography not available at the time of publication.

Daan Roos received the B.Sc. and M.Sc. degrees (*cum laude*) in electrical engineering from the Delft University of Technology (TU Delft), Delft, The Netherlands, in 2021 and 2024, respectively. He is currently working toward the Ph.D. degree in electrical engineering with the Terahertz Sensing Group, TU Delft and Space Research Organisation Netherlands, SRON, Leiden, The Netherlands.

His current research interests include passive cameras, quasi-optical systems, and superconducting detectors.

Dimitry Lamers, photograph and biography not available at the time of publication.

Daniela Perez Capelo received the B.Sc. degree in chemical science and engineering from the University of Twente, Enschede, The Netherlands, in 2021.

She is currently a Cleanroom Process Engineer with the Nano-Lithography Team, Space Research Organization Netherlands (SRON) Leiden, The Netherlands, by assessing high yield fabrication routes for MKIDs. Her research interests include lithography, materials science, and nanotechnology.

Hendrik M. Veen, photograph and biography not available at the time of publication.

David J. Thoen, photograph and biography not available at the time of publication.

Vishal Anvekar received the bachelor of Engineering (B.E.) degree in electronics and communications from Vishweshwaraiah Technological University, Belgaum, India, in 2009, and the Doctor of Philosophy (Ph.D.) degree in nanotechnology from the Indian Institute of Technology Bombay, Mumbai, India, in 2017.

He is currently with Instrument Science Group—Nano, Space Research Organisation Netherlands (SRON), Leiden, The Netherlands, on various microfabrication projects for different space missions. His research interests include plasmonics, microfabrication of MEMS and other optical microdevices, thin film process development, and superconductor detectors and *LC* filters.

Stephen J. C. Yates received the Ph.D. degree from the University of Bristol, Bristol, U.K., in 2003.

He has been an Instrument Scientist with the Space Research Organisation Netherlands (SRON), Leiden, The Netherlands, since 2006. He was with the CNRS-CRTBT (now Institut Neél) Grenoble, Grenoble, France, on Experimental Low Temperature Physics (2003–2006). He has authored or coauthored 80 papers. His current interests concentrate on MKID development for sub-mm to FIR astronomical applications but also include a wider interest in device physics and superconductivity, optics, and full end to end instrument characterization and performance.

Willem Jellema received the M.Sc. degree in applied physics from the University of Groningen, Groningen, The Netherlands, in 1998, and the Ph.D. degree in applied physics, with a focus on the optical design and performance verification of Herschel-HIFI, from the Faculty of Mathematics and Natural Sciences, University of Groningen, in 2015.

He has been a Senior Instrument Scientist with the Space Research Organisation Netherlands (SRON), Groningen, The Netherlands, since 1998. From 1998 to 2015, he was an Instrument Scientist involved with the Herschel-HIFI project, responsible for the end-to-end optical design verification, alignment, and calibration. Since 2009, he has been an Instrument Scientist of SPICA-Safari, a far-infrared spectrometer proposed for a large aperture cryogenic telescope in space. In 2014, he became the Lead Systems Engineer of SPEX, an optical multiangle spectropolarimeter for future atmospheric missions. In 2017, he temporarily moved to NOVA to support the development of the METIS, MICADO, and MOSAIC instruments for the E-ELT as an (Optical) Systems Engineer. In 2018, he returned to SRON in his role as an Instrument Scientist for SPICA-Safari. He has been involved in various other projects related to the development, engineering, and calibration of submillimeter-wave and optical instrumentation for space. His research interests include long-wave diffractive optics and coherent heterodyne technologies and applications.

Robert Huiting, photograph and biography not available at the time of publication.

Lorenza Ferrari received the Ph.D. degree in applied physics, with a focus on cryogenic detectors for astrophysics applications, from the University of Genoa, Genoa, Italy, in 2009.

After that, she was with the INFN, Genoa, Italy, and PTB, Berlin, Germany, for one year, as a Postdoctoral Researcher involved with low temperature detectors for neutrino mass experiments. Since 2010, she has been an Instrument Scientist with SRON-Space Research Organisation Netherlands, Leiden, The Netherlands. Her current interests include the development of microwave kinetic inductance detectors for sub-mm applications and transition edge sensors for FAR-IR frequency range, focussing on optical characterization and application in scientific instruments. She is also involved in the SpicA FAR-Infrared Instrument and X-ray Integral Field Unit Spectrometer experiments modeling and testing the focal plane assembly, as well as designing cryogenic facilities for performance validation of instruments components.

Carole Tucker, photograph and biography not available at the time of publication.

Sven L. Van Berkel (Member, IEEE) received the M.Sc. degree in electrical engineering and the Ph.D. degree (*cum laude*) in electromagnetics from the Delft University of Technology (TU Delft), Delft, The Netherlands, in 2015 and 2020, respectively.

His Ph.D. research focused on passive THz imaging systems, ultrawideband antennas for (sub)millimeter-wave applications, quasi-optical systems, analytical/numerical techniques in electromagnetics, and transmission line characterization. From 2020 to 2022, he was a NASA Postdoctoral Program Fellow with the Submillimeter-Wave Advanced Technology Group, NASA Jet Propulsion Laboratory (JPL), California Institute of Technology, Pasadena, CA, USA, where he developed lens-coupled antennas, absorbers, and phased arrays for terahertz/infrared heterodyne/direct-detection spectroscopy instruments. From 2022 to 2025, he continued that work as an RF Microwave Engineer with NASA JPL. Since 2025, he has been a Submillimeter-waves Engineer with the European Space Agency (ESA) ESTEC, Noordwijk, The Netherlands, contracted via Akkodis Netherlands.

Dr. Van Berkel was a recipient of the 2020 Dutch Vederfonds Vederprijs and the 2024 IETE Sri C Viswanatha Reddy Memorial Award.

Peter K. Day received the B.S. degree in physics from the University of California, Berkeley, Berkeley, CA, USA, in 1988 and the Ph.D. degree in physics from the California Institute of Technology, Pasadena, CA, USA, in 1993.

He has been with the Jet Propulsion Laboratory, Pasadena, CA, USA, since 1996. He is currently a Leverhulme Visiting Professor with the University of Oxford, Oxford, U.K., and visiting fellow with Brasenose College, Oxford, U.K. His main research interests are superconducting detectors and amplifiers.

Henry George Leduc received the B.S. degree in physics from Montana State University, Bozeman, MT, USA, in 1977, and the M.A. and Ph.D. degrees in physics from the University of California, Davis, CA, USA, in 1983.

Since 1983, he has been with Jet Propulsion Laboratory, California Institute of Technology, Pasadena, CA, USA, where he is currently a Senior Research Scientist. His research has been centered around superconducting devices and sensors.

Charles M. Bradford, photograph and biography not available at the time of publication.

Nuria Llombart (Fellow, IEEE) received the master's degree in electrical engineering and the Ph.D. degree in electromagnetics from the Polytechnic University of Valencia, Valencia, Spain, in 2002 and 2006, respectively.

During her master's degree studies, she spent one year with the Friedrich Alexander University of Erlangen Nuremberg, Erlangen, Germany, and was with the Fraunhofer Institute for Integrated Circuits, Erlangen, Germany. From 2002 to 2007, she was with the Antenna Group, TNO Defense, Security and Safety Institute, The Hague, The Netherlands, working as a Ph.D. Student and afterward as a Researcher. From 2007 to 2010, she was a Postdoctoral Fellow with the SubmillimeterWave Advance Technology Group, Jet Propulsion Laboratory, California Institute of Technology, Pasadena, CA, USA. She was a "Ramón y Cajal" Fellow with the Optics Department, Complutense University of Madrid, Madrid, Spain, from 2010 to 2012. In 2012, she was with the THz Sensing Group, Technical University of Delft, Delft, The Netherlands, where she has been a Full Professor since 2018. She has coauthored more than 200 journal and international conference contributions in the areas of antennas and terahertz systems.

Dr. Llombart was the corecipient of the H. A. Wheeler Award for the Best Applications Paper of 2008 in IEEE TRANSACTIONS ON ANTENNAS AND PROPAGATION, the 2014 THz Science and Technology Best Paper Award of the IEEE Microwave Theory and Techniques Society, and several NASA awards. She was also the recipient of the 2014 IEEE Antenna and Propagation Society Lot Shafai Mid-Career Distinguished Achievement Award. In 2015, she was the recipient of European Research Council Starting Grant. She is a Board Member of the International Society of Infrared, Millimeter, and Terahertz Waves and, since 2023, the Editor in Chief of IEEE TRANSACTIONS ON THZ SCIENCE AND TECHNOLOGY. In 2019, she was appointment IEEE Fellow for contributions to millimeter and submillimeter wave quasi-optical antennas.

Jochem J. A. Baselmans received the Graduate and Ph.D. (*summa cum laude*) degrees in physics from the University of Groningen, Groningen, The Netherlands, in 1998 and 2002, respectively.

He is currently a Senior Instrument Scientist with the Space Research Organisation Netherlands, (SRON), Leiden, The Netherlands, and a Full Professor in Experimental Astronomy with the THz Sensing Group, Delft University of Technology, Delft, The Netherlands. He started in 2002 as a Postdoctoral Instrument Scientist with SRON Netherlands Institute for Space Research, where has worked until 2004 on Hot Electron Bolometer mixers. Since then, he leads the Dutch effort on Kinetic Inductance Detectors. He pioneered the concept of the on-chip spectrometer for far-infrared radiation detection and is a Lead System Engineer for the first on-chips spectrometer instrument, Deshima. He is also the Detector Lead for the AMKID camera on APEX and has pushed MKID technology to sensitivity levels suitable for future cryogenically cooled space-based observatories. During his Ph.D., he studied the superconducting state in normal metal Josephson junctions. He has authored or coauthored more than 100 papers.